



Calhoun: The NPS Institutional Archive
DSpace Repository

Theses and Dissertations

1. Thesis and Dissertation Collection, all items

1983

Observations of inertio-gravity waves in the wake of hurricane Frederic.

Shay, Lynn K.

Monterey, California. Naval Postgraduate School

<http://hdl.handle.net/10945/19924>

Downloaded from NPS Archive: Calhoun



Calhoun is the Naval Postgraduate School's public access digital repository for research materials and institutional publications created by the NPS community. Calhoun is named for Professor of Mathematics Guy K. Calhoun, NPS's first appointed -- and published -- scholarly author.

Dudley Knox Library / Naval Postgraduate School
411 Dyer Road / 1 University Circle
Monterey, California USA 93943

<http://www.nps.edu/library>

NAVAL POSTGRADUATE SCHOOL

Monterey, California



THESIS

OBSERVATIONS OF INERTIO-GRAVITY WAVES IN THE
WAKE OF HURRICANE FREDERIC

by

Lynn K. Shay

December 1983

Thesis Advisor:

R. L. Elsberry

Approved for public release; distribution unlimited.

T215693

REPORT DOCUMENTATION PAGE		READ INSTRUCTIONS BEFORE COMPLETING FORM
1. REPORT NUMBER	2. GOVT ACCESSION NO.	3. RECIPIENT'S CATALOG NUMBER
4. TITLE (and Subtitle) Observations of Inertio-Gravity Waves in the Wake of Hurricane Frederic		5. TYPE OF REPORT & PERIOD COVERED Master's Thesis; December 1983
		6. PERFORMING ORG. REPORT NUMBER
7. AUTHOR(s) Lynn Keith Shay		8. CONTRACT OR GRANT NUMBER(s)
9. PERFORMING ORGANIZATION NAME AND ADDRESS Naval Postgraduate School Monterey, CA 93943		10. PROGRAM ELEMENT, PROJECT, TASK AREA & WORK UNIT NUMBERS
11. CONTROLLING OFFICE NAME AND ADDRESS Naval Postgraduate School Monterey, CA 93943		12. REPORT DATE December 1983
		13. NUMBER OF PAGES 120
14. MONITORING AGENCY NAME & ADDRESS (if different from Controlling Office)		15. SECURITY CLASS. (of this report) Unclassified
		15a. DECLASSIFICATION/DOWNGRADING SCHEDULE
16. DISTRIBUTION STATEMENT (of this Report) Approved for public release, distribution unlimited		
17. DISTRIBUTION STATEMENT (of the abstract entered in Block 20, if different from Report)		
18. SUPPLEMENTARY NOTES		
19. KEY WORDS (Continue on reverse side if necessary and identify by block number) hurricane Frederic, inertio-gravity waves, inertial waves, group velocity, phase velocity, normal modes, barotropic, baroclinic, complex demodulation, least squares, Brunt Vaisala frequency		
20. ABSTRACT (Continue on reverse side if necessary and identify by block number) Inertial waves excited in the mixed layer by hurricane Frederic, had horizontal scales of approximately 1 to 2 times the baroclinic Rossby radius of deformation (50 km) of the first mode near the DeSoto Canyon. Initially, energy propagated vertically at about 1.25 km/d and horizontally at about 80 km/d. These waves spun down over e-folding scales of four inertial periods as energy propagated vertically at 270 m/d and horizontal-		

ly at 30 km/d. Inertio-gravity waves in the deep thermocline had horizontal scales of 25 to 50 km and vertical scales approximately equal to the water depth. The energy of these waves was dominated by the barotropic mode with some contributions from modes 1 and 2. These waves were not admitted to the shelf region because the bottom slope was greater than the slope of the internal wave characteristics.

The mean flow followed the isobaths at all levels, but it was in the opposite direction in the bottom layer. The mean flow initially decreased along the eastern boundary of the canyon as the storm forcing readjusted the flow. Near-bottom temperature variations of 4°C were associated with the storm surge and advection in the along-track direction, particularly along the north rim of the canyon.

Approved for public release; distribution unlimited

Observations of Inertic-Gravity Waves in the Wake of
Hurricane Frederic

by

Lynn K. Shay
B.S. Oceanography, Florida Institute of Technology, 1976

Submitted in partial fulfillment of the
requirements for the degree of

MASTER OF SCIENCE IN OCEANOGRAPHY

from the

NAVAL POSTGRADUATE SCHOOL
December 1983

ABSTRACT

DUPLICATE LIBRARY
NATIONAL CENTER FOR
MONTEREY, CALIFORNIA 93943

Inertial waves excited in the mixed layer by hurricane Frederic, had horizontal scales of approximately 1 to 2 times the baroclinic Rossby radius of deformation (50 km) of the first mode near the DeSoto Canyon. Initially, energy propagated vertically at about 1.25 km/d and horizontally at 80 km/d. These waves spun down over e-folding scales of four inertial periods as energy propagated vertically at 270 m/d and horizontally at 30 km/d. Inertio-gravity waves in the deep thermocline had horizontal scales of 25 to 50 km and vertical scales approximately equal to the water depth. The energy of these waves was dominated by the barotropic mode with some contributions from modes 1 and 2. These waves were not admitted to the shelf region because the bottom slope was greater than the slope of the internal wave characteristics.

The mean flow followed the isobaths at all levels, but it was in the opposite direction in the bottom layer. The mean flow initially decreased along the eastern boundary of the canyon as the storm forcing readjusted the flow. Near-bottom temperature variations of 4°C were associated with the storm surge and advection in the along-track direction, particularly along the north rim of the canyon.

TABLE OF CONTENTS

I.	INTRODUCTION	13
II.	HISTCRICAL REVIEW	16
III.	DATA AND ANALYTICAL METHODS	23
	A. CURRENT METER DATA	23
	B. STCFM TRACK	24
	C. WIND FIELD	27
	D. VERTICAL TEMPERATURE GRADIENTS	27
	E. TEMPCRAL AND SPATIAL SCALES	30
	F. CCMPUTATION OF SFECTRA	32
	G. COMFLEX DEMODULATION	34
IV.	STORM PEFIOD	37
	A. INERTIAL RESPONSE	37
	B. SUBINERTIAL RESPCNSE	63
	C. SUPEFINERTIAL RESPONSE	73
V.	NORMAL MODES	81
	A. THECRY	81
	B. DATA ANALYSIS	83
VI.	CONCIUSICNS	95
APPENDIX A.	98
	A. CCMFLEX DEMODULATION	98
	B. POTENTIAL ENERGY	100
	C. LEAST SQUARES FIT	101

APPENDIX E.	104
A. DEEP REGION	104
B. SHALLOW REGION	110
LIST OF REFERENCES	115
INITIAL DISTRIBUTION LIST	118

LIST OF FIGURES

Figure 1.	Track of Hurricane Frederic.	14
Figure 2.	Satellite Photograph of Frederic at 2001 GMT 12 Sept. 1979.	26
Figure 3.	Wind Speed and Direction Measured by NOAA Buoy 42003.	28
Figure 4.	Vertical Temperature and Brunt-Vaisala Frequency Profiles.	30
Figure 5.	Frequency Response for the Band-pass and Low-pass Filters.	36
Figure 6.	Band-Pass Filtered Mixed layer V Velocity Component at CMA3.	36
Figure 7.	Mixed Layer Velocity Components at CMA2. . .	38
Figure 8.	Similar to Fig. 7, except at CMA3.	40
Figure 9.	Time Series of HKE in the Mixed layer	41
Figure 10.	Similar to Fig. 8, except in the deep thermocline (251 m)	43
Figure 11.	Progressive Vector Diagrams at CMA3.	44
Figure 12.	Time Series of HKE at CMA3	47
Figure 13.	Normalized HKE Spectra from CMA3	49
Figure 14.	Mixed Layer Normalized Rotary Spectra from CMA3	50
Figure 15.	Vertical Scales at CMA3	55
Figure 16.	Estimates of Horizontal Scales in the Mixed Layer	58
Figure 17.	Horizontal Scales in the Deep Thermocline . .	60
Figure 18.	Low-pass Filtered PVD at CMA2.	66
Figure 19.	Low-pass Filtered PVD at CMA3.	67

Figure 20.	Thermocline Temperature Time Series from CMA3 at 251 m.	69
Figure 21.	Temperature Time Series from CMA2 at 324 m.	71
Figure 22.	Pctential Energy Spectra from CMA3	72
Figure 23.	Crcss-Spectrum Between V-Velocity and Temperature	75
Figure 24.	Mid-depth Velccity Ccmpnents from CMA1. . .	76
Figure 25.	Horizontal Velccity Eigenfunctions at 29.33 N and 87.11 W.	84
Figure 26.	V Velocity Coefficients at CMA3	86
Figure 27.	Same as Fig. 26, except at CMA2.	87
Figure 28.	V Component Time Series at CMA3	93
Figure 29.	Surface PVD fcr a) CMA2 and b) CMA3. . . .	105
Figure 30.	Bottcm PVD for a) CMA2 and b) CMA3. . . .	106
Figure 31.	Temperature Time Series from CMA3 at 457 m.	111
Figure 32.	Mid-depth PVD at CMA1.	112

LIST OF TABLES

TABLE I.	Comparison of Inertial-Internal Wave Parameters	17
TABLE II.	A Synopsis of Storm Period Observations . .	25
TABLE III.	Rossby Radii of Deformation	32
TABLE IV.	Normalized Rotary Spectrum Analysis at Inertial Frequency	51
TABLE V.	Vertical and Horizontal Coherencies at the Inertial Frequency	53
TABLE VI.	Comparison of Vertical and Horizontal Group Velocity.	61
TABLE VII.	Normalized Rotary Spectrum Analysis at Subinertial Frequency	70
TABLE VIII.	Normalized HKE Spectra at Inertial and Semi-diurnal Frequency	77
TABLE IX.	Normalized Rotary Spectra at the Semi- diurnal Frequency.	79
TABLE X.	Variance of the Normal Modes at CMA2 and CMA3.	90
TABLE XI.	Normalized HKE Spectral Estimates at 95% Confidence	107
TABLE XII.	Normalized Rotary Spectrum Analysis . . .	109
TABLE XIII.	Normalized HKE Spectral Estimates at 95% Confidence	113

ACKNOWLEDGEMENT

The author extends his gratitude to all those who have contributed to the evolution of this thesis. First and foremost, I would like to express my deepest appreciation to my faculty advisor, Prof. Russell Elsberry. His guidance and wisdom during a very difficult time of my life were exceeded only by his thorough knowledge of the subject matter. Under his leadership, this thesis work has been the crescendo of my graduate education. The expertise of Dr. Andrew Willmott is held in high regard. His attention to mathematical details has made this thesis a much better manuscript. I also wish to thank Prof. Christopher Mooers for his willingness to share his knowledge on the application of normal mode theory to the analysis of current meter data, and for providing the computer program, IWEG, to solve for the vertical structure. His criticism and advice have contributed significantly to my development as an oceanographer. The wisdom and guidance of Dr. William Hart whenever encouragement was needed has also been greatly appreciated.

The dedicated efforts of the personnel who maintain the computer systems at the W. R. Church Computer Center at NPS as well as at NAVOCEANO are greatly appreciated. Their work certainly helped expedite the publishing of this thesis.

I also wish to acknowledge the unheralded efforts of the current meter group of NAVOCEANO. In particular, the fine work of Messrs. Jose Alonso and Steve Clark is appreciated and have made this thesis work a reality. The advice of Drs. Bill Wiseman (LSU), Zack Hallock (NORDA), and Ben Korgen (NAVOCEANO) and Mr. Jack Tamul (NAVOCEANO) was extremely helpful in the analysis of the data. Drs. Hank Perkins (NORDA) and Ortwin von Zwick (NAVOCEANO) have shared some stimulating ideas concerning inertial-internal wave motions. I further extend my gratitude to Mr. Jerry Carroll for his assistance in gaining access to this very unique data set. The Physical Oceanography Branch at NAVOCEANO kindly provided some of the computer software used in the data analysis. The expertise of Mr. Steve Lauber in the pre-processing of the data greatly aided the data analysis. The drafting of some of the figures was done with great care by Ms. Viola Luttrell, Mr. Chuck Murphy, and Mr. Glenn Voorhis of NAVOCEANO.

I thank the two most important people in my life, my wife, Sally and daughter, Missy. Their patience and encouragement during the evolution of the thesis has helped me a great deal.

Finally, I would like to thank NAVOCEANO for their support over the first three quarters of my graduate studies. Furthermore, the author extends his appreciation to ONR for support during the final stages of the research.

I. INTRODUCTION

" the deer alone learneth "

Nietzsche.....

The oceanic response to intense, transient atmospheric events, such as hurricanes, is dominated by robust inertial wave excitation in the mixed layer and the subsequent propagation and dispersion of inertio-gravity waves in the thermocline. The study of these forced waves has been largely through numerical and analytical investigations, because of the lack of sufficient data to resolve the scales and energetics of the motion. Hence, observations of ocean currents and temperatures during a hurricane are necessary for validating models and theories dealing with forced inertio-gravity waves.

A comprehensive data set of ocean observations was collected by the U. S. Naval Oceanographic Office (NAVOCEANO) during the passage of hurricane Frederic in the summer of 1979 (Shay and Tamul, 1980). NAVOCEANO deployed three moored taut-wire current meter arrays in the northern Gulf of Mexico southeast of Mobile, Alabama. During the period of deployment, hurricane Frederic passed within 80 to 130 km

of the array sites (Fig. 1) at 2100 GMT 12 September. Five hours later, Frederic made landfall at Dauphin Island, Alabama. During and subsequent to the passage of Frederic, the National Hurricane Research Division dropped several expendable bathythermographs (AXBT) from reconnaissance aircraft in the area of the current meter deployments (Black, 1983).

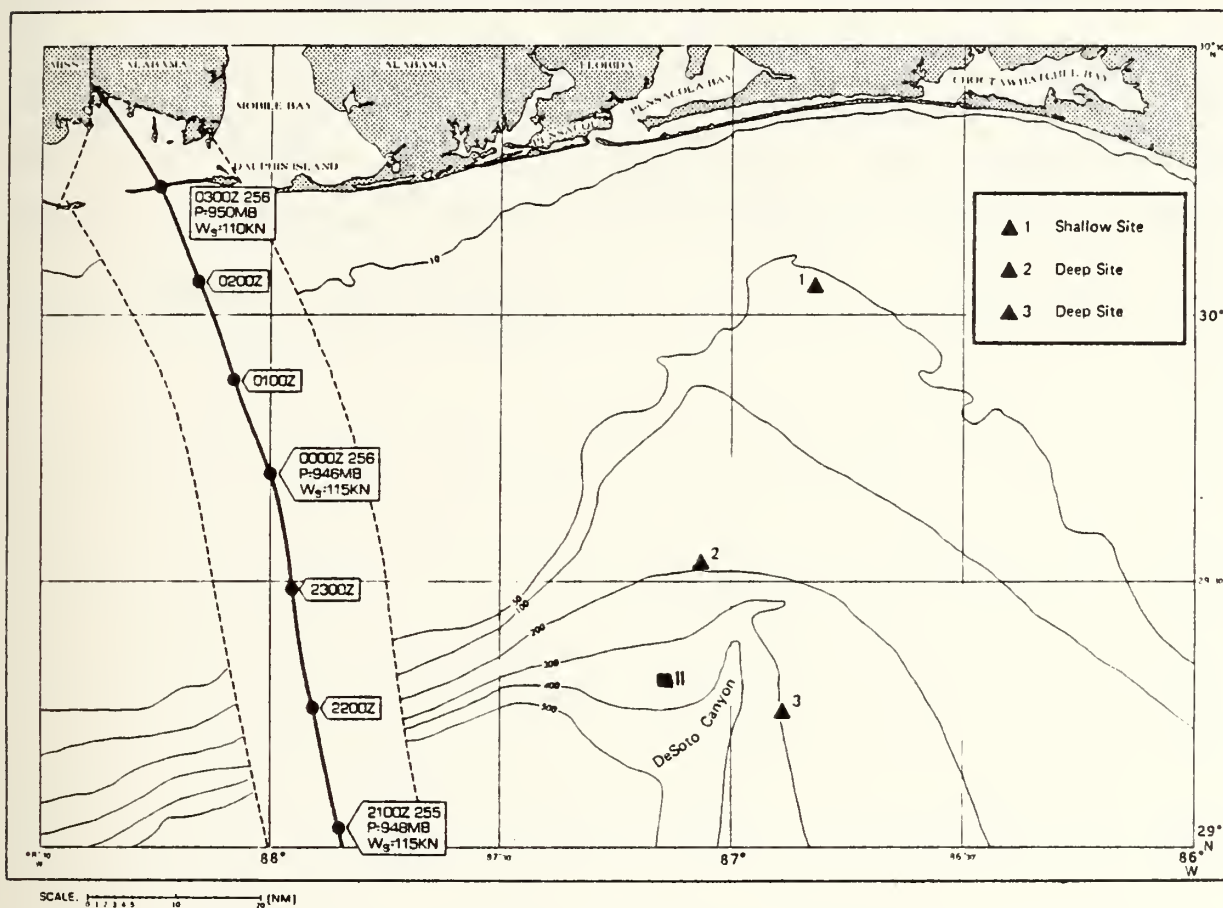


Figure 1. Track of Hurricane Frederic. The contours are in fathoms, ▲ depicts positions of current meter arrays, (NAVOCEANO), ■ depicts the position of AXBT drops (Black, 1983). The track of hurricane Frederic is based on a report by Hebert (1979).

This thesis addresses the problem of the vertical and horizontal dispersion of the forced inertial wave energy from the mixed layer. The forcing readjusts the mean flow as well as generating anisotropic inertial motion. The current meter observations allow determination of the scales and the energetics of the forced, anisotropic wave motion through use of spectrum analysis and complex demodulation. The modal structure is examined by formulating the Sturm-Liouville problem and then performing a least squares fit between the eigenfunctions and the demodulated time series of the current observations.

II. HISTORICAL REVIEW.

A nonlinear model for a stationary hurricane (O'Brien and Reid, 1967) was developed to simulate the observations made in the wake of hurricane Hilda (Leipper, 1967). The results indicated that upwelling regions were restricted to the area enclosed by the maximum wind regime, whereas downwelling occurred outside this regime as warm water was advected away from the storm center.

One of the most pronounced responses of the ocean to wind forcing is the generation of inertial oscillations in the surface mixed layer. Pollard (1970) simulated the generation of these waves using a two-dimensional, wind-driven model developed by Pollard and Millard (1970). The predicted amplitudes and decay rates of the forced oscillations agreed well with the Woods Hole Oceanographic Institution (WHOI) 'site D' observations. Using the same data set, Pollard (1980) showed that under relatively strong wind conditions, 67 % of the horizontal kinetic energy (HKE) in the mixed layer was found near the inertial frequency. The subsequent downward propagation of energy was estimated to be

of the order of 10^{-3} cm/s (1 m/d). This vertical group velocity was too small to account for the radiation of inertial waves and the subsequent loss of energy from the mixed layer. The corresponding scales of the inertial wave motion were about 100 to 240 m in the vertical and hundreds of kilometers in the horizontal (Table I).

TABLE I
Comparison of Inertial-Internal Wave Parameters

Length	Brooks (1983)	Price (1983)	Pollard (1980)
Scales			
Horizontal (km)	370	480	700-1700
Vertical (m)	1000	1000	100-240
Group Velocity			
Horizontal (km/d)	23	86	0.8-17.
Vertical (m/d)	60	160	0.03-3.
From Brooks (1983)			

Using a linear, two-layer model, Geisler (1970) simulated inertic-gravity waves as part of the baroclinic response in the wake of a translating storm. The critical factors governing the generation of these waves were:

- the translational speed of the hurricane must be greater than the internal wave phase speed; and
- the horizontal scales of these waves must be comparable to the oceanic Rossby radius of deformation.

He further noted that the ocean response to a moving hurricane is strongly baroclinic.

The ocean thermal response to hurricane forcing, was investigated numerically by imposing Ekman layer dynamics in a mixed layer model (Elsberry et al., 1976). The input of energy from the wind stress was forced to generate inertial oscillations and cause turbulent mixing via entrainment. Upwelling also enhances the turbulent mixing process in the upper layers of the ocean. The main result was that advection dominated the thermal response near the storm track as opposed to the heat loss from the ocean surface to the storm.

Strong atmospheric forcing enhances the turbulent mixing process in the surface mixed layer and causes it to deepen. As the mixed layer continues to deepen, the thermocline begins to erode as water from the thermocline is entrained into the mixed layer. However, stratification tends to suppress turbulent mixing and aids in the creation of small-scale internal waves either through entrainment or Kelvin-Helmholtz instabilities (KH) at the base of the mixed layer (Pollard et al., 1973 ; Garwood, 1977) .

Below the mixed layer, ocean current variability is linked to vertically propagating wave groups of the internal wave field (Kase and Olbers, 1979). The actual mechanisms for the vertical transport of energy from the wind forced mixed layer to the thermocline for the generation of large scale inertial-internal waves are not well understood. Perhaps the most effective way of creating these large scale inertial-internal waves is through Ekman suction. Krauss (1972 a,b, 1976) showed that a horizontally varying wind stress causes a mass transport 90 deg. to the right of the stress in the Ekman surface layer. This surface layer divergence is accompanied by an upward displacement of the isopycnals or upwelling of colder water from below which tends to suppress the turbulent mixing process. During the relaxation of the wind, these isopycnals are displaced downward, which contributes to the creation of large scale inertial-internal waves at the base of the mixed layer.

During the passage of hurricane Belle (Mayer et al., 1981), ocean current and temperature measurements were acquired on the continental shelf of the Middle Atlantic Bight. Their analyses indicated that most of the inertial-internal wave energy was contained in the first mode at the

deeper sites (water depth of 70 m) and in a heavily damped second mode at the shallow sites (water depth of 50 m). The variability in the modes was not attributed to the spatial variability of the wind stress. The bottom slope and mean velocity fields significantly altered the oceanic response to hurricane Felle.

A mixed layer model (Garwood, 1977) was embedded into a multi-layer, primitive equation, ocean circulation model (GCM) by Adamec et al., (1980). Using this GCM model, Hopkins (1982) simulated the baroclinic response to a forcing pattern similar to hurricane Frederic and compared the results to the data collected in the wake of Frederic (Shay and Tamul, 1980). The model predicted the inertial response in the mixed layer quite well. However, the predicted ocean current response in the subsurface layers was less energetic than the observations, and decayed much too fast. These discrepancies between the model simulations and observations are due in part to the imposition of the rigid lid condition at the surface, which eliminates the barotropic mode. Furthermore, these model simulations did not include topography, even though the observations are from a region where the bottom topography is rugged and the ocean depth is less than 1 km deep.

Recently, ocean measurements were made during the passage of hurricane Allen in the western Gulf of Mexico (Brocks, 1983). The spatial scales of the inertial wave were different from the 'site D' observations, as shown in Table I. The vertical scales in the ocean are generally much greater under hurricane forcing than during the passage of a cold front, while the converse is true for the horizontal scales of motion. The vertical group velocity, which depends on both the wave and the Brunt-Vaisala frequencies, for the Allen observations exceeded the group velocity from the 'site D' observations. This estimate from the Allen observations is misleading due to the lack of upper thermocline and mixed layer data. Moreover, the wind speed is much greater during the passage of a hurricane than a frontal passage. Therefore, the amount of turbulent mixing in the mixed layer and inertial wave excitation should be much more rapid during a hurricane. Other features measured in the Allen response included topographical dependence, and the vertical phase locking during the first few inertial period (IP) following the storm.

The baroclinic response of the ocean to a hurricane was modeled by (Price, 1983) using a multi-level, inviscid

model. The scales and energetics of the simulated inertial response were similar to mixed layer data collected by a NOAA data buoy during the passage of hurricane Eloise. The horizontal and vertical scales, as given in Table I, were quite large in comparison to the thickness of the thermocline (200 m). The maximum energy of the inertial-internal wave motion was predicted to occur at a distance of twice the radius of maximum winds, hereafter referred to as the maximum wind regime, which was roughly 80 km for Eloise. Further, the rate of vertical energy propagation was large in comparison to both the Allen and 'site D' observations, and accounted for the depletion of energy from the mixed layer. Other mechanisms, such as KH instability (Pollard et al., 1973 ; Garwood, 1977) and turbulence (Bell, 1978), act to remove energy from the mixed layer. However, these phenomena were neglected as mixing was not explicitly included in the model formulation.

Greatbatch (1983) modeled the nonlinear response of the ocean to a moving storm. The major results were that the transition between upwelling and downwelling zones in the oscillatory wake was rapid, and that nonlinearities account for the displacement of the maximum response to the right of the storm track.

III. DATA AND ANALYTICAL METHODS

A. CURRENT METER DATA

Ten Aanderaa RCM-5 current meters were deployed on three moored taut-wire arrays in depths ranging from 100 to 470 m in the northern Gulf of Mexico. These current meters sampled ocean current speed, direction and temperatures at 10 minute intervals. Two current meter arrays (CMA2, and 3) were deployed on adjacent sides of the DeSoto Canyon where bathymetric contours converge to form the head of the canyon (see Fig. 1). The other mooring was deployed closer to the coast in a depth of about 100 m of water where the isobaths are nearly parallel to the coast. A synopsis is given in Table II of the storm period observations, which extends from a few days prior to hurricane passage (12 September) to the end of the deployment period (mid-October).

The quality of the data is generally good; however, the lengths of the time series are not all the same. For instance, the Savonius rotors were eventually lost from all current meters in the mixed layer due to the large current speeds. These large mixed layer current speeds are not

corrected for rotor pumping, which is a function of the mooring design as well as the large direction vane of the Aanderaa current meters (Fofonoff and Ercan, 1967). In addition to the rotor problems, temperature records from all mixed layer current meters were unrecoverable because the ocean temperature exceeded the threshold temperature of the thermistors of 21.5 °C. Sea surface temperatures 325 km south-southeast of the mooring sites, as measured by NOAA Buoy 42003, reached 28.8°C (Johnson and Renwick, 1981).

B. STORM TRACK

The storm track is based on the best position data on hurricane Frederic's movement through the Gulf of Mexico (Hebert, 1979). Because of the intensity of Frederic, reconnaissance aircraft constantly monitored the storm. Frederic increased to maximum strength, maximum winds or minimum barometric pressure, 80 to 130 km west of the CMA sites about 2100 GMT 12 September (see Fig. 1). A visible photograph of Frederic from a GOES satellite at 2001 GMT 12 September clearly delineates a well developed eye of about 40 to 50 km in diameter (Figure 2). The translational speed of the hurricane at this time was about 7 to 7.5 m/s as it approached the Gulf Coast, which was much larger than the

internal wave phase speed. Thus, an inertio-gravity wave response is expected in the wake of hurricane Frederic (Geisler, 1970).

TABLE II
A Synopsis of Storm Period Observations

Meter Depth (m)	Reccrd Length (days)	Start Time (GMT)	End Time (GMT)	Variables
<u>CMA1</u>				
21	0	No hurricane data		
49	22.21	0040 5 Sep.	0600 27 Sep.	u,v
64	16.76	0040 5 Sep.	1920 21 Sep.	u,v,T
92*	20.79	0040 5 Sep.	2040 25 Sep.	u,v,T
<u>CMA2</u>				
19	24.67	0040 5 Sep.	1650 29 Sep.	u,v
179	22.63	1920 7 Sep.	0100 30 Sep.	u,v,T
324	24.76	0040 5 Sep.	1900 29 Sep.	u,v,T
<u>CMA3</u>				
21	24.91	0100 2 Sep.	2200 26 Sep.	u,v
251	36.00	0100 2 Sep.	0100 8 Oct.	u,v,T
437	35.69	0100 2 Sep.	1730 7 Oct.	u,v,T
457	31.94	0100 2 Sep.	0000 4 Oct.	u,v,T

* time clock synchronization problems
u,v = horizontal velocity components
T = temperature
GMT = Greenwich Mean Time

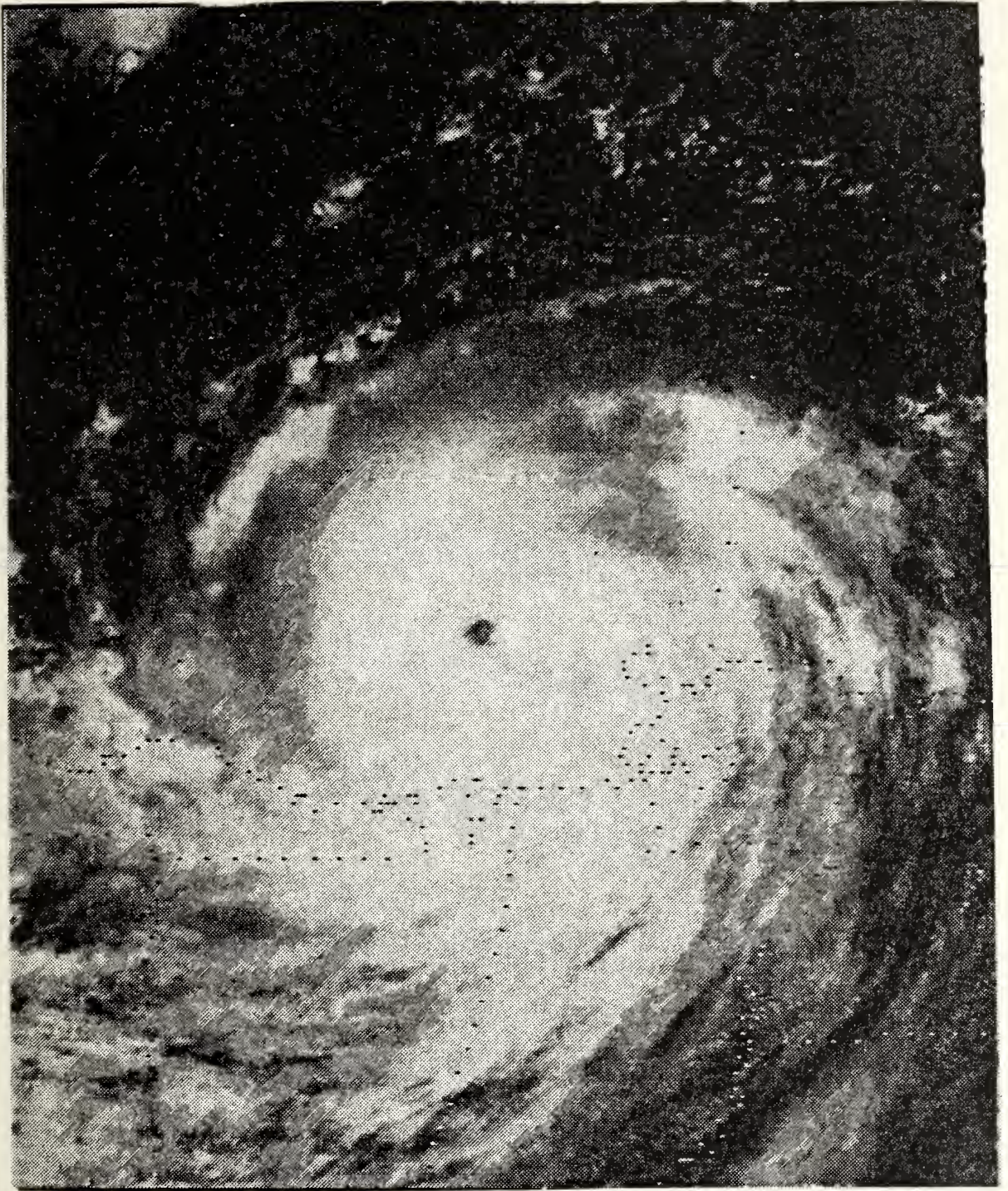


Figure 2. Satellite Photograph of Frederic at 2001 GMT 12 Sept. 1979. Visual satellite imagery is courtesy of NOAA/NESDIS.

C. WIND FIELD

Wind field data were obtained from shore stations at Mobile, Alabama and Pensacola, Florida. These records indicated that the surface wind speed did not exceed 40 m/s. However, other reports suggested that wind speeds ranged between 48 to 58 m/s as Frederic made landfall (Hebert, 1979). These discrepancies are attributed to local boundary effects and the non-representativeness of wind data collected in the coastal region. Marine winds were also measured by NOAA Buoy 42003 (Johnson and Renwick, 1981). Wind speeds at this location never exceeded 35 m/s. The eye clearly passed over the buoy as indicated by the minimum in the wind field as the direction changed from 40 to 200 ° True (Fig. 3), with a corresponding decrease in pressure to 959 millibars (mb).

D. VERTICAL TEMPERATURE GRADIENTS

The AXBT data collected by the National Hurricane Research Division, as reported by Black (1983), are used for the computation of the Brunt-Vaisala frequency. These data were collected after the passage of Frederic in the area of current meter array deployments near the DeSoto Canyon (see Fig. 1).

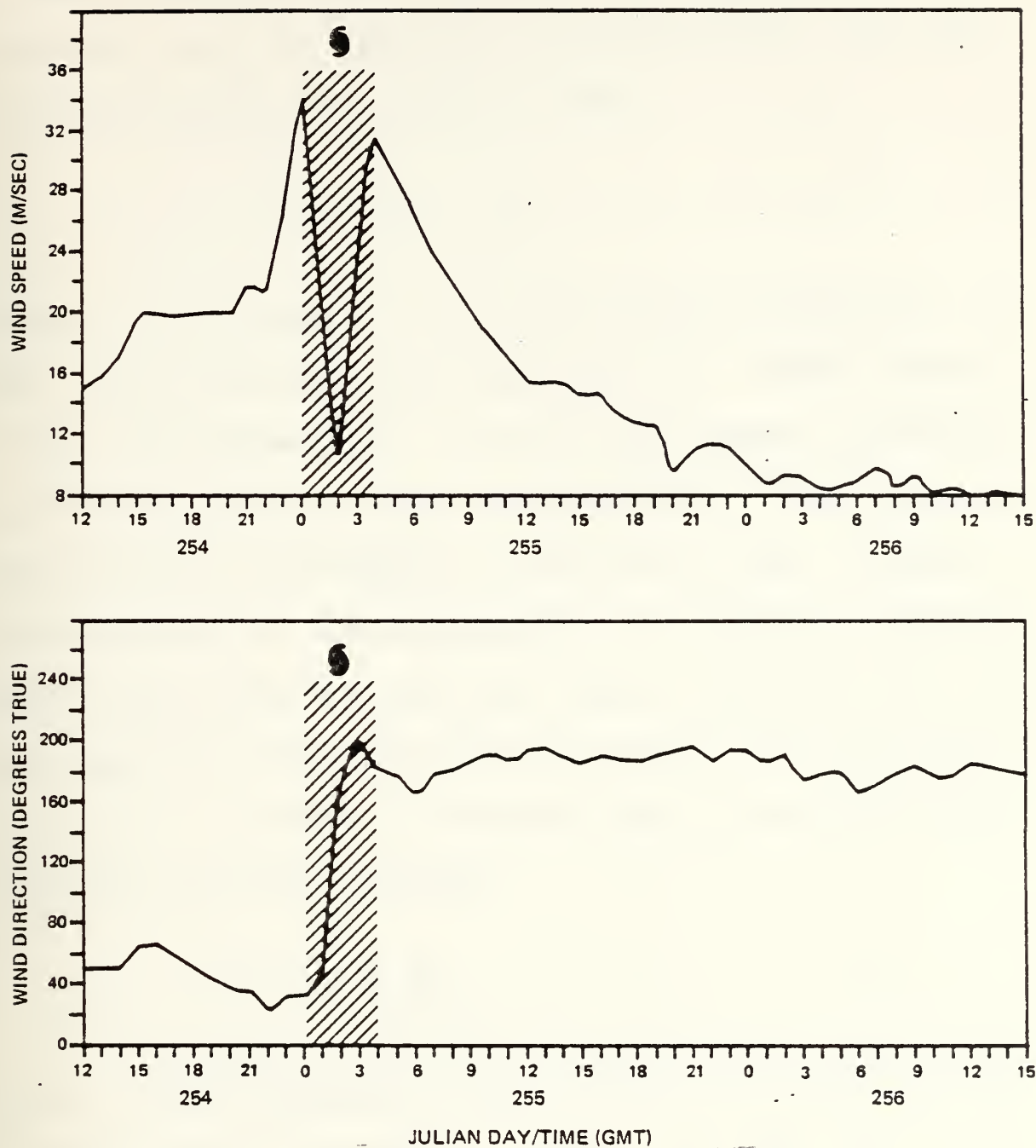


Figure 3. Wind Speed and Direction Measured by NOAA Buoy 42003. The upper panel represents the observed wind speed time series where the abscissa depicts time in Julian Days starting on 1200 GMT 11 Sept. to 1500 GMT 13 Sept. 1979. The lower panel represents the concurrent wind direction time series. The hatched area depicts the period when the data buoy was in the eye of the hurricane (Johnson and Renwick, 1981).

The vertical density profiles are computed at 10 m intervals using the AXBT data and climatological data from NAVOCEANO through the equation of state

$$\rho = \rho_0(1 - \alpha(T - T_0)) \quad ? \quad (1)$$

where ρ is the density, T is the observed temperature, T_0 and ρ_0 are the reference temperature and density respectively from climatology, and α is the thermal expansion coefficient, which is taken to be $0.0002/^\circ\text{C}$. Some error is expected due to the neglect of the salinity term. However, an examination of the climatological T-S diagram, for the DeSoto Canyon area indicates that density variations are due to temperature rather than salinity effects. The Brunt-Vaisala, N^2 , frequency is computed using a centered finite difference from the expression

$$N^2 = - \frac{g}{\rho_0} \frac{\Delta \rho}{\Delta z} \quad ? \quad (2)$$

where g is the acceleration due to gravity and $\Delta \rho / \Delta z$ is the vertical density gradient. Since the AXBT data only extended to about 250 m, it was necessary to extrapolate the vertical temperature gradient to 470 m. The temperature is

assumed to decrease uniformly at a rate of $0.0311\text{ }^{\circ}\text{C/m}$ from 250 to 470 m (Fig. 4). The corresponding uniform increase in the density produces a constant Brunt-Vaisala profile.

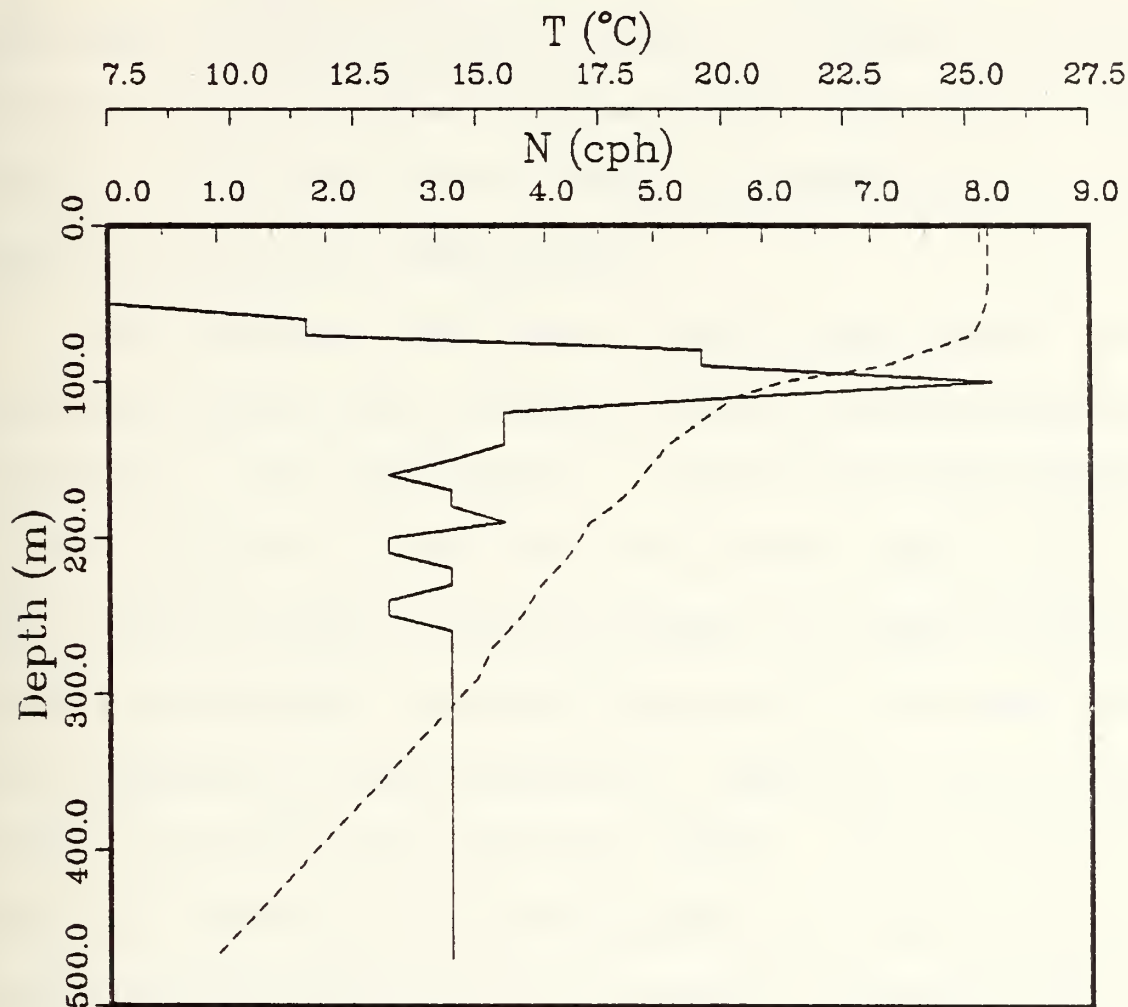


Figure 4. Vertical Temperature and Brunt-Vaisala Frequency Profiles. The abscissa depicts the Brunt-Vaisala frequency (solid) and temperature (dashed) from Black (1983).

E. TEMPORAL AND SPATIAL SCALES

The local variations in the bottom topography at the DeSoto Canyon (see Fig. 1) are approximately parallel and

normal to the coast at CMA2 and CMA3. For example, north-south flow at CMA2 is in the cross-shelf direction, but it is in the along-shelf direction at CMA3. Henceforth, a Cartesian coordinate system is used to represent the horizontal velocity components in the x and y directions, where motion to the east and the north corresponds to $+u$ and $+v$ current velocities, respectively.

The fundamental time scale used in this thesis is an inertial period, which is equal to 24.10, 24.25 and 24.47 h at CMA 1, 2 and 3 respectively. In the following calculations, the Inertial Period (IP) will be set equal to 24.4 h. The intrinsic length scales are either the radius of maximum winds, approximately 40 km for Frederic, or the Rossby radii of deformation, which are given in Table III for the barotropic and first three baroclinic modes. These deformation radii are based on the inertio-gravity wave phase speed computed from the Sturm-Liouville problem, which will be discussed in a later section. For convenience, the scales in the x and y directions will be referenced as cross and along-track scales respectively, because the storm track was nearly perpendicular to the coastline.

TABLE III
Rossby Radii of Deformation

Mode No.	Phase Speed (m/s)	Deformation Radii (km)
0	68.0	950.
1	4.0	56.
2	2.2	30.
3	1.3	18.

F. COMPUTATION OF SPECTRA

The energy and cross spectra are computed in the following manner: (1) the mean is computed and is extracted from the time series; (2) a Tukey data window is applied to the data; (3) the data are transformed into frequency space via the Fast Fourier Transform (FFT); and (4) the transformed data are spectrally averaged over bandwidths which vary in width with frequency, and are closely tied to the computation of confidence levels. The number of data points transformed by the FFT used in the spectrum analyses does not have to be proportional to 2^n , where n is an integer. The general FFT is advantageous in the analysis of events because of their transient nature. However, in the analysis of the spectra, equal numbers of data points are used to avoid leakage and smearing of energy from adjacent frequency

bands (Otnes and Enochson, 1978) . Finally, the higher frequency energy above the Nyquist frequency, $1/(2 \Delta t)$ where Δt is the sampling interval, is eliminated to prevent aliasing of the spectra.

The HKE is decomposed into the clockwise (CW) and counterclockwise (CCW) rotating components using the rotary spectrum method outlined in Gonella (1972) and Mooers (1973). The main results of this analysis are the rotary spectrum, ellipse stability and orientation, and rotary coefficient. The orientation of the ellipse indicates the direction of the horizontal phase velocity, while the stability indicates the variability in the ellipse orientation. A high stability index indicates that the wave motion is anisotropic, or that the horizontal direction of phase propagation is unidirectional. Conversely, a low index of stability implies that the direction of phase propagation is random or isotropic. The rotary coefficient indicates the amount of confidence that can be placed in the rotary spectral estimate and the rotational component that dominates the rotary spectrum. For instance, a +1.00 implies that the motion is polarized in the CW direction. A more rigorous mathematical treatment is given by Gonella (1972) and Mooers (1973).

G. COMPLEX DEMODULATION

A useful method for determining inertial oscillations in a time series of ocean current measurements is through the use of the complex demodulation method (Perkins, 1970). The mathematical details are given in Appendix A. This method can be implemented either by linear filtering or by performing a least squares harmonic analysis on the time series. The linear filtering method is preferred because data points are lost whenever harmonic analyses are used to form the time-varying amplitudes and phases of frequency dependent motions. This is especially useful in the analysis of events when all data points are needed to resolve the transient motions. A major disadvantage of the linear filtering method is that it only applies to discrete frequencies, whereas the least squares method can treat all frequencies within the constraints of the time series.

Initially, the data are band-pass filtered between 18 and 30 h to limit the frequency content in the time series to near-inertial motions. These filtered data are multiplied by the trigonometric arguments of the inertial frequency. At this point, some higher frequency motions have been introduced into the time series (Appendix A) and these

are removed by low-pass filtering the data at 22 h. The resultant time series is manipulated to form the instantaneous amplitudes and phases of the inertial motion. The final set of time-varying amplitudes and phases provide a local harmonic analysis, or more explicitly, a time series of spectral estimates for inertial motion. The filter used in the demodulation was a Lanczos square taper window with 241 weights (Fig. 5).

The band-pass filtered, mixed layer velocity components at CMA3 are excellent examples for using complex demodulation (Fig. 6). As the current velocities increase in response to the storm, the amplitude of the forced inertial wave increases as well. The inertial wave amplitudes modulate the increases and decreases in the mixed layer velocities. After the maximum velocities occur, roughly 2 IP following hurricane passage, the strength of the currents decreases linearly with e-folding scales of about 4 IP. This type of e-folding behavior is very common in amplitude-modulated signals.

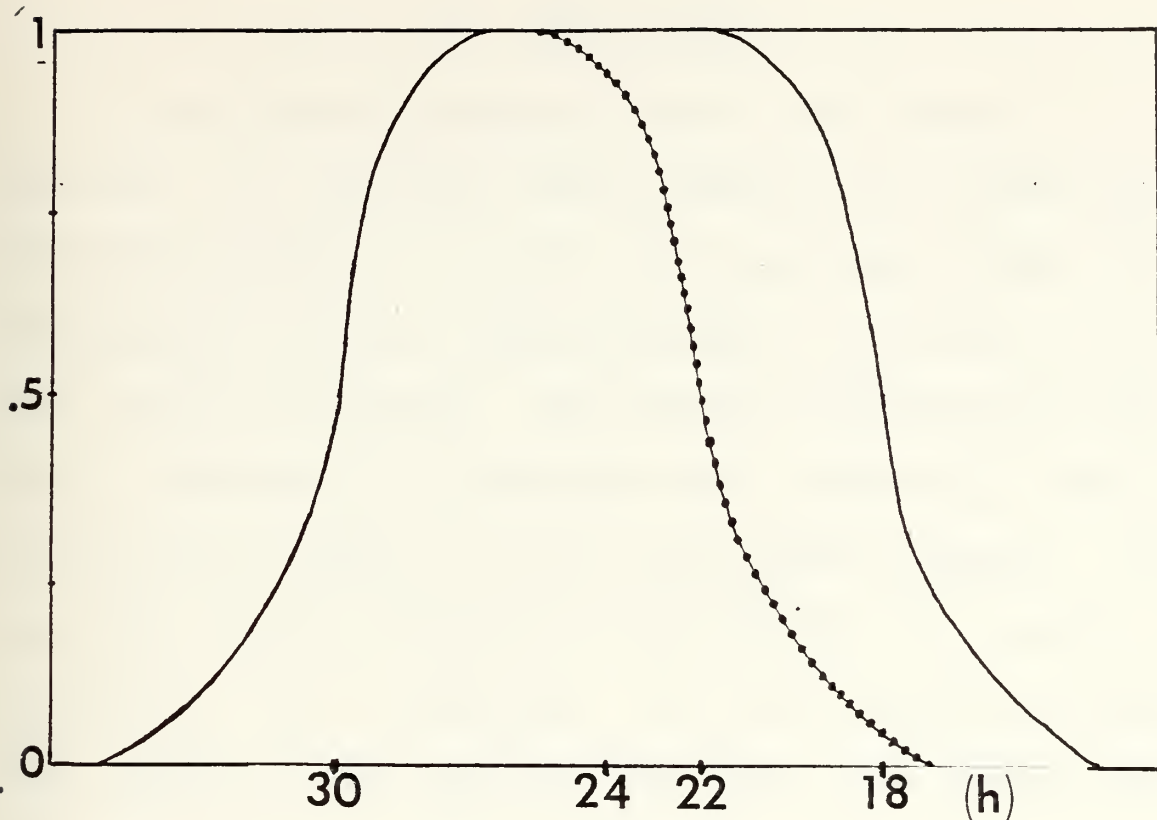


Figure 5. Frequency Response for the Band-pass and Low-pass Filters. The band-pass filter response is represented by the solid line while the low-pass filter response is shown by the dotted line.

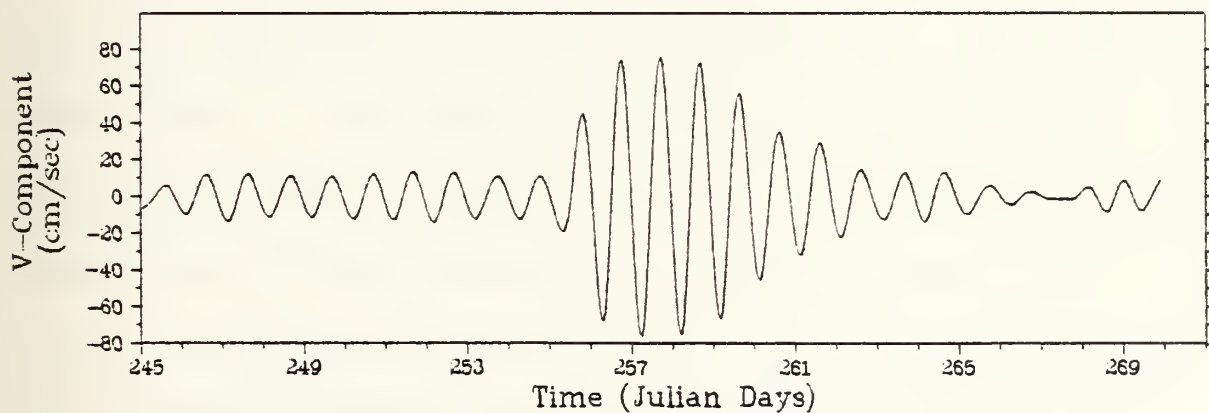


Figure 6. Band-Pass Filtered Mixed layer V Velocity Component at CMA3.

IV. STORM PERIOD

In the following analyses, the data are divided into two periods: 1) the storm period observations as previously described in Table II; and 2) the quiescent period which encompasses the period from the start of the data to a few days prior to the storm. This chapter focuses on the inertial, subinertial and superinertial response in terms of energetics and scales of motion to hurricane Frederic. The quiescent period observations and results are given in Appendix B. For convenience, the terms shallow and deep will refer to the regions where CMA1 and CMA2,3 were deployed.

A. INERTIAL RESPONSE

Hurricane Frederic passed about 80 km west of the DeSoto Canyon at 2100 GMT 12 September (JD 255) 1979. The current speeds began to increase at 0700 GMT or approximately 14 h prior to the time of closest approach. The currents in the mixed layer at CMA2 increased to a maximum within an IP following the passage of Frederic (Fig. 7). The storm caused the horizontal velocity to oscillate with periods of about 24.3 h and to rotate in a CW direction, which indicates the

presence of inertial waves in the mixed layer. These waves then decreased in amplitude over e-folding scales of 4 IP. The storm also caused the u-component to flow in the opposite direction from that of the pre-storm flow, whereas the v-component increased markedly in amplitude. The near-bottom current speeds (shown later) began to increase within 3 h after the mixed layer response.

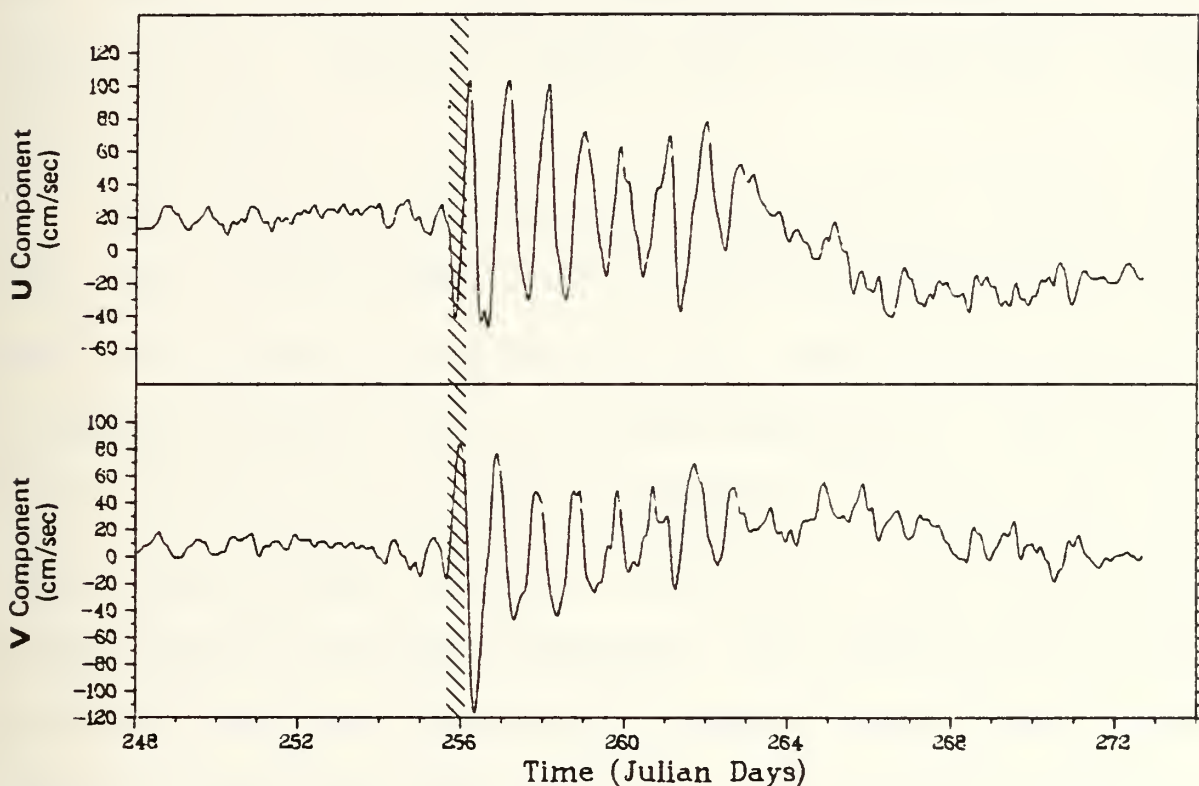


Figure 7. Mixed Layer Velocity Components at CMA2. The ordinate depicts the magnitude of the horizontal velocity components in cm/s for the east-west current (upper) and north-south current (lower). The hatched area depicts the period of hurricane passage.

In the mixed layer at CMA3, the storm amplified the pre-storm currents to a maximum of 135 cm/s (Fig. 8). As at CMA2, this increase in the currents is a manifestation of inertial wave excitation. However, the inertial response at CMA3 was different from CMA2 in that the kinetic energy of the waves was larger and persisted longer (approximately 2 IP). The energy of these waves then decreased over e-folding scales of 4 IP. The increase in near-bottom current (shown later) occurred within 4.5 h following the mixed layer response.

These horizontal differences of the inertial response in the mixed layer between CMA2 and CMA3 are observed in the amplitude changes of the HKE (Fig. 9). The initial increase in kinetic energy at the two arrays was similar. The maximum in kinetic energy occurred first at CMA2 and led the mixed layer maximum at CMA3 by about 3 h. The differences in HKE levels were quite pronounced. For example, the mixed layer HKE level was roughly 60 % of that found in the mixed layer at CMA3, even though CMA2 was closer to the eye of the storm. This large difference over a distance of 34 km may be due in part to the stronger mean current at CMA2, which may have reduced the amplitude of the inertial waves. The

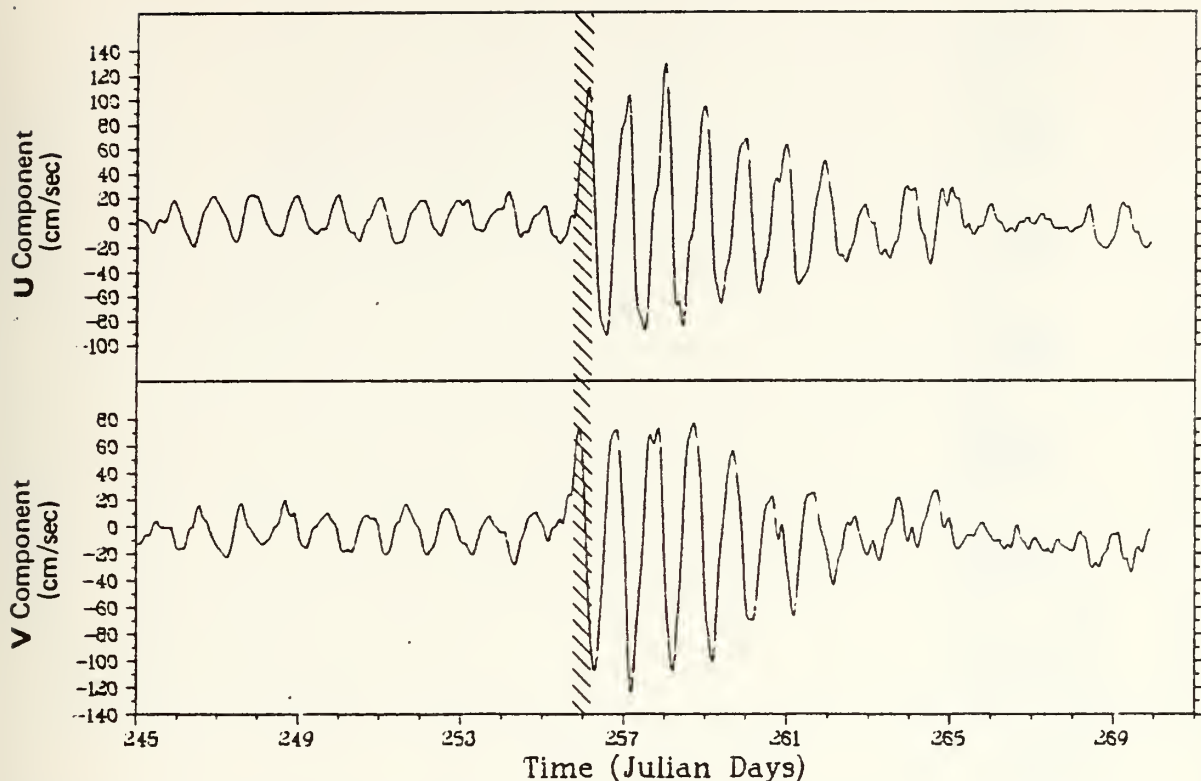


Figure 8. Similar to Fig. 7, except at CMA3.

direction of the mean flow and the horizontal phase propagation of the inertial waves (shown below) roughly coincided, which suggests that there may have been some interaction between them. Following these maxima, the energy decayed with an e-folding scale of 4 IP at both arrays. Forced inertial waves in the mixed layer that vary in space and time are one mechanism to drive inertio-gravity waves in the subsurface layers (Krauss, 1972a,b).

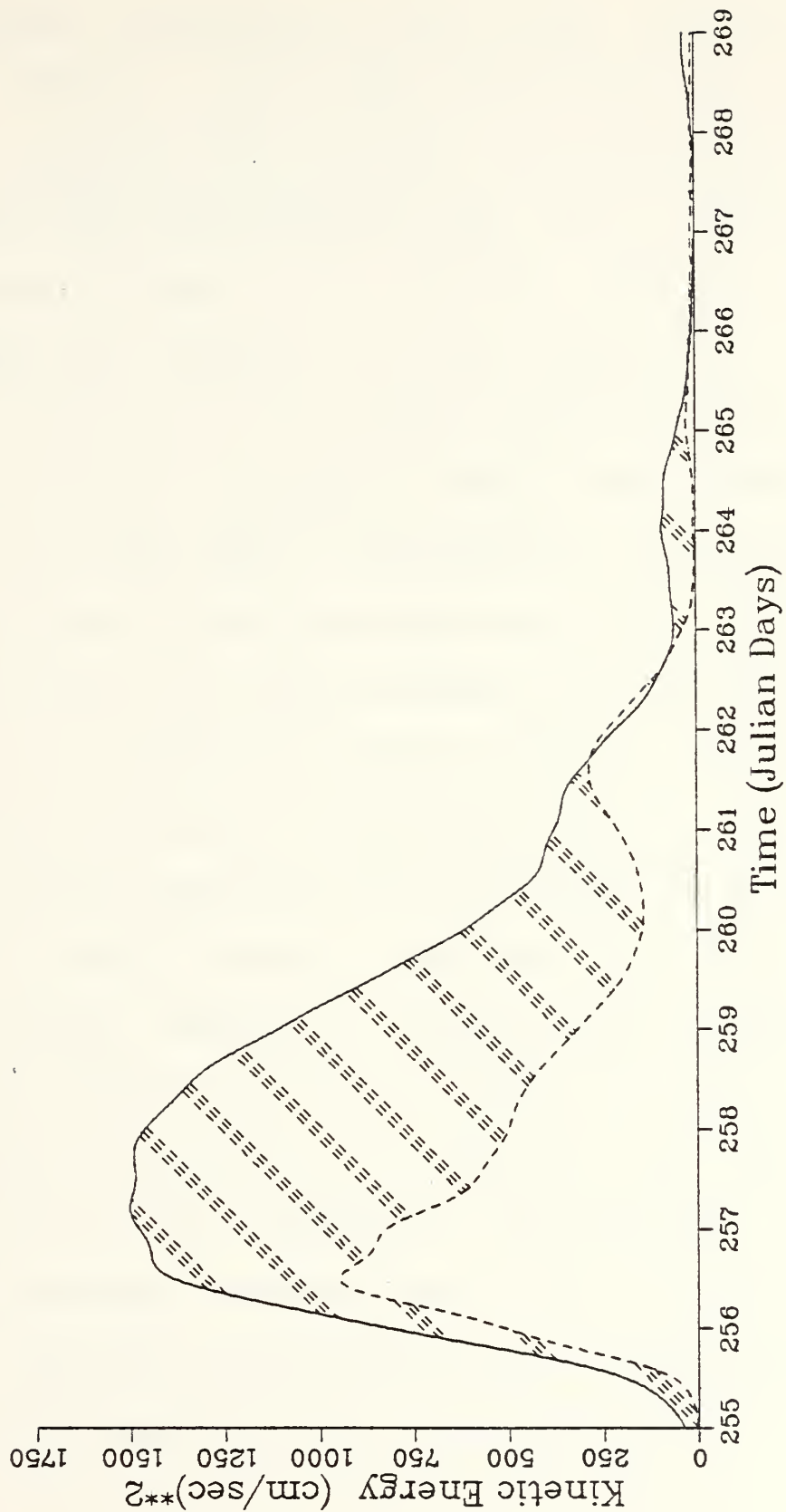


Figure 9. Time Series of HKE in the Mixed layer at CMA3 (solid) and at CMA2 (dashed).

The vertical differences in the inertial response were even more dramatic. In the deep thermocline (251 m) at CMA3, the increase in the currents was sensed within 2 h following the mixed layer response (Fig. 10). The initial maximum occurred within an IP (JD 256) after the winds relax, which was followed by inertial oscillations in the horizontal currents. In the presence of stratification, the particle motions are elliptical rather than circular as observed in the mixed layer. The amplitude of inertio-gravity waves decreased slightly following the initial response. About 10 IP later, the current increased to a secondary maximum that nearly exceeded the initial maximum. The u-velocity essentially defined an amplitude-modulation envelope that collapsed and expanded in time and persisted for 21 IP following the initial maximum. The near-bottom currents at CMA3 (shown later) behaved in a similar manner except that the secondary maximum occurs 6 IP following the storm.

The vertical changes in the currents at CMA3 are even more apparent in the progressive vector diagrams (PVD), which are Lagrangian representations of the Eulerian measurements. That is, the continuous current measurements are integrated with respect to time to approximate the

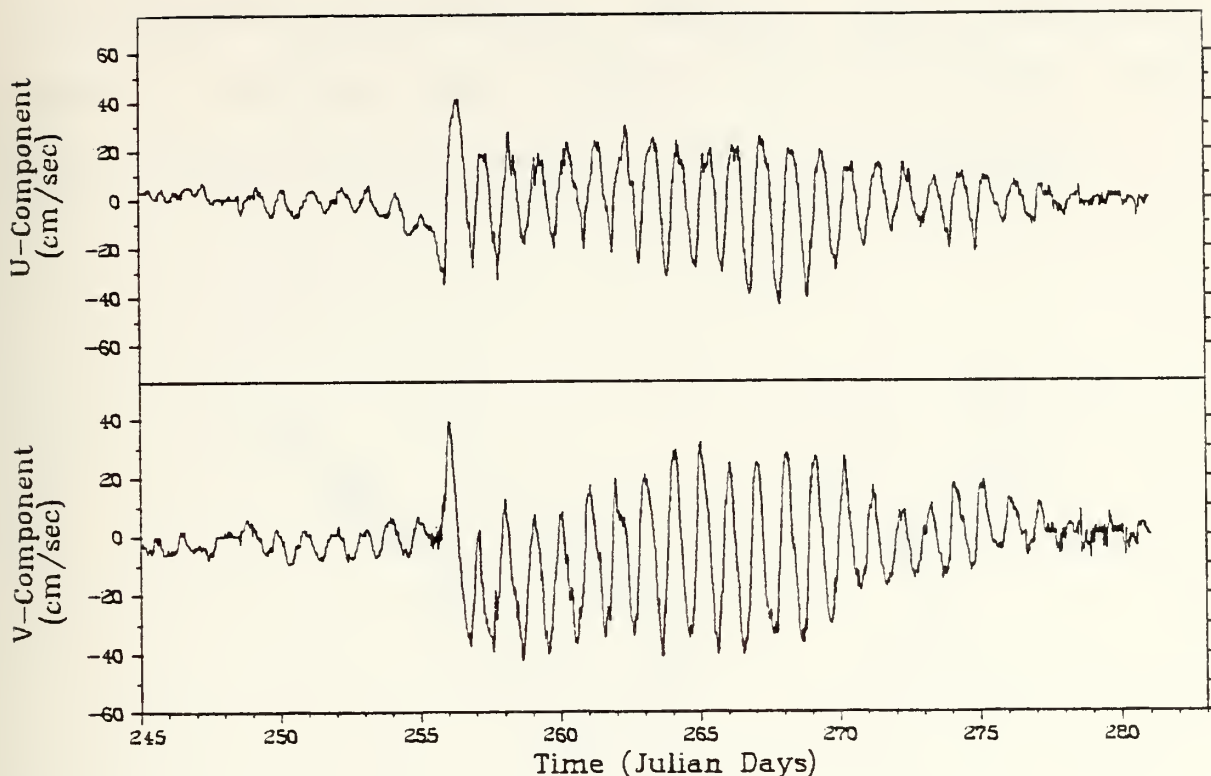


Figure 10. Similar to Fig. 8, except in the deep thermocline (251 m).

trajectory of the water parcels at that point. The horizontal velocity components in the mixed layer at CMA3 definitely showed the classical, CW rotating vector associated with inertial waves (Fig. 11a). Prior to the storm, small scale, freely propagating inertial waves were present, and they were subsequently amplified in response to the storm. These forced waves were superposed on a southward mean flow that increased in magnitude in response to the forcing. The horizontal displacement over successive time intervals of 2

IP increased following storm passage. After the maximum current velocities near JD 258, the amplitude of these forced, near-circular inertial oscillations decreased.

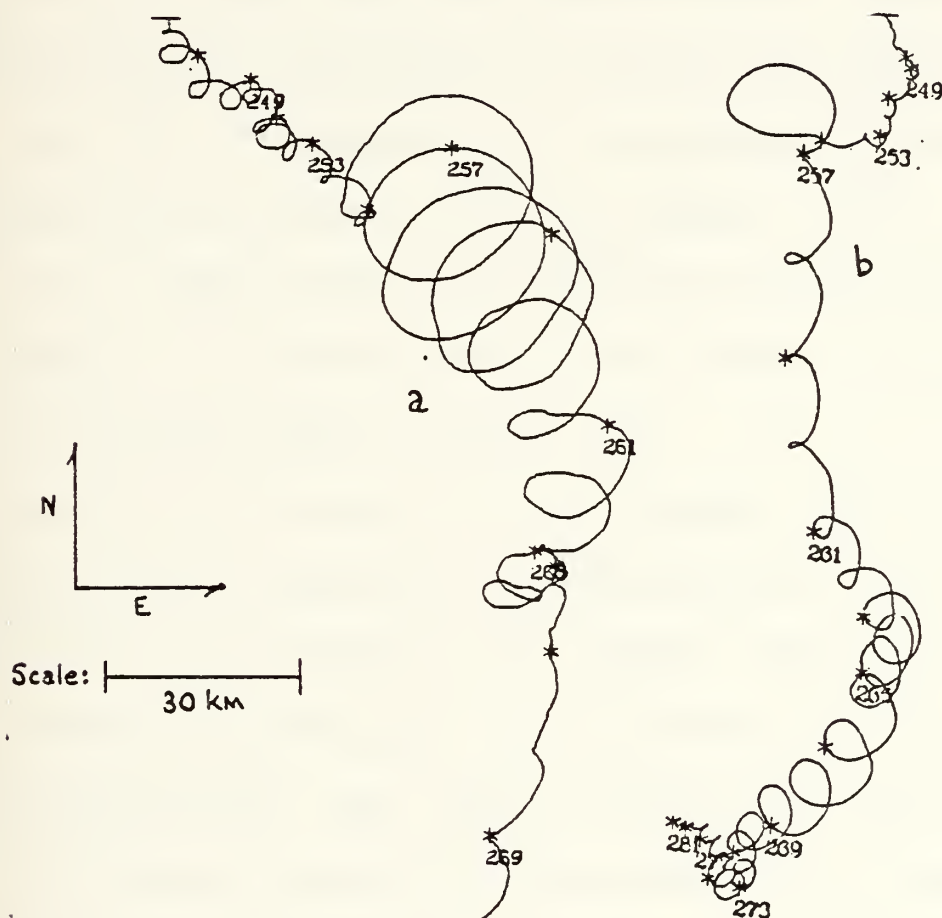


Figure 11. Progressive Vector Diagrams at CMA3. The * represents a time span of 48 h starting on JD 245 for a) mixed layer (21 m), and b) the deep thermocline (251 m).

In the thermocline (Fig. 11b), the storm amplified the freely propagating inertio-gravity waves. However, the dimensions of the ellipses are distorted because of the increases in the mean flow between JD 257 and 261. This period was immediately followed by decreases in the mean flow until JD 265, when the inertio-gravity response was more pronounced. The period of increasing and then decreasing mean flow corresponds to the approximate modulation envelope and lag period of 10 IP between JD 256 and 266 (Fig. 10). After JD 266, the modulation envelope started to collapse as the inertio-gravity waves decayed in amplitude with an e-folding scale of about 4 IP.

The vertical propagation of the energy, which is a consequence of the generation of inertio-gravity waves in the thermocline, is indicated by the vertical differences in the HKE between the mixed layer and the thermocline (Fig. 12). In the mixed layer, the maximum HKE occurred approximately one IP following the storm and persisted over the next 2 IP. Subsequently, a relative maximum was reached in the deep thermocline about 2 h after the surface maximum, and it was only 5 to 8 % of the maximum HKE in the mixed layer. Based only on these initial phase differences between the velocity

components at the two levels, the vertical propagation of energy would be about 3 cm/s (2.6 km/d). The thermocline HKE then remained nearly constant over the next 4 to 6 IP. On JD 262, the thermocline HKE gradually began to increase as the vertically propagating energy from the mixed layer accumulated. Using this 10 IP lag period, the vertical propagation of energy is about 0.03 cm/s (26 m/d). The first estimate of 2.6 km/d is about 1 to 2 orders of magnitude greater than the Eloise and Allen observations (see Table I). However, the second estimate of 26 m/d is much more comparable to the Allen estimates. The propagation of energy will be addressed below using the dispersion relation of inertio-gravity waves. The phase propagation was clearly upward over the first 10 IP following the storm. Over the subsequent 10 IP, the propagation was not as clear as phases in the mixed layer became erratic, presumably due to the decreasing energy levels or spectral broadening.

The inertial peak dominated the HKE spectra at both locations and at all depths. The change in the inertial HKE between the surface and bottom layers was about an order of magnitude, while the energies between mid-depth and intermediate levels did not change significantly at CMA3 (Fig. 13).

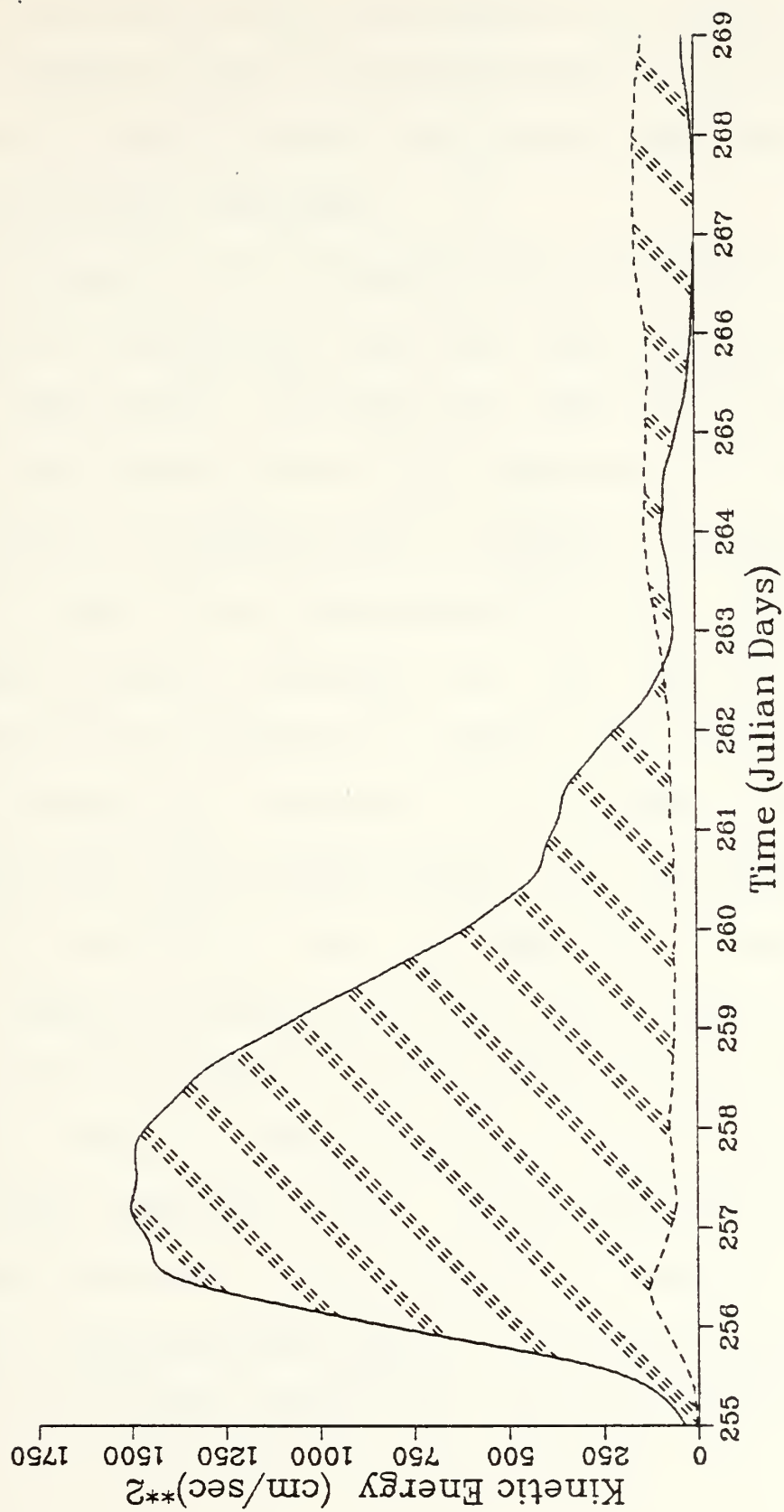


Figure 12. Time Series of HKE at CMA3 for the mixed layer (solid) and the thermocline (dashed). The hatched area depicts the vertical difference in the HKE.

Although the inertial peak was prominent, the variability in spectral shapes was due to the differences in the background continuum of internal waves which varies with depth (Fu, 1980) and bandwidth averaging.

The HKE spectra are decomposed into CW and CCW rotating components to clarify the rotational characteristics of the inertial wave motion. The spectral peak near the inertial frequency was shifted about 3-6% higher than the inertial frequency and it dominated the CW spectra calculated from the mixed layer velocity measurements at CMA3 (Fig. 14). The rotary spectrum estimates for the inertial period motions are given in Table IV. The CW, inertial HKE variability estimates are generally 1 to 2 orders of magnitude larger than the CCW rotating motion. In comparison, the subinertial (periods of 3 IP) and superinertial (periods of 12 h) CW spectral estimates are more than an order of magnitude less than the inertial motion (Tables VII and VIII).

At all levels at the deep region, the positive rotary coefficients approached unity, which indicates that the waves were polarized in the CW direction (Table IV). The direction of the semi-major axes of the inertial ellipses at CMA2 rotated CW with depth except near the bottom. The

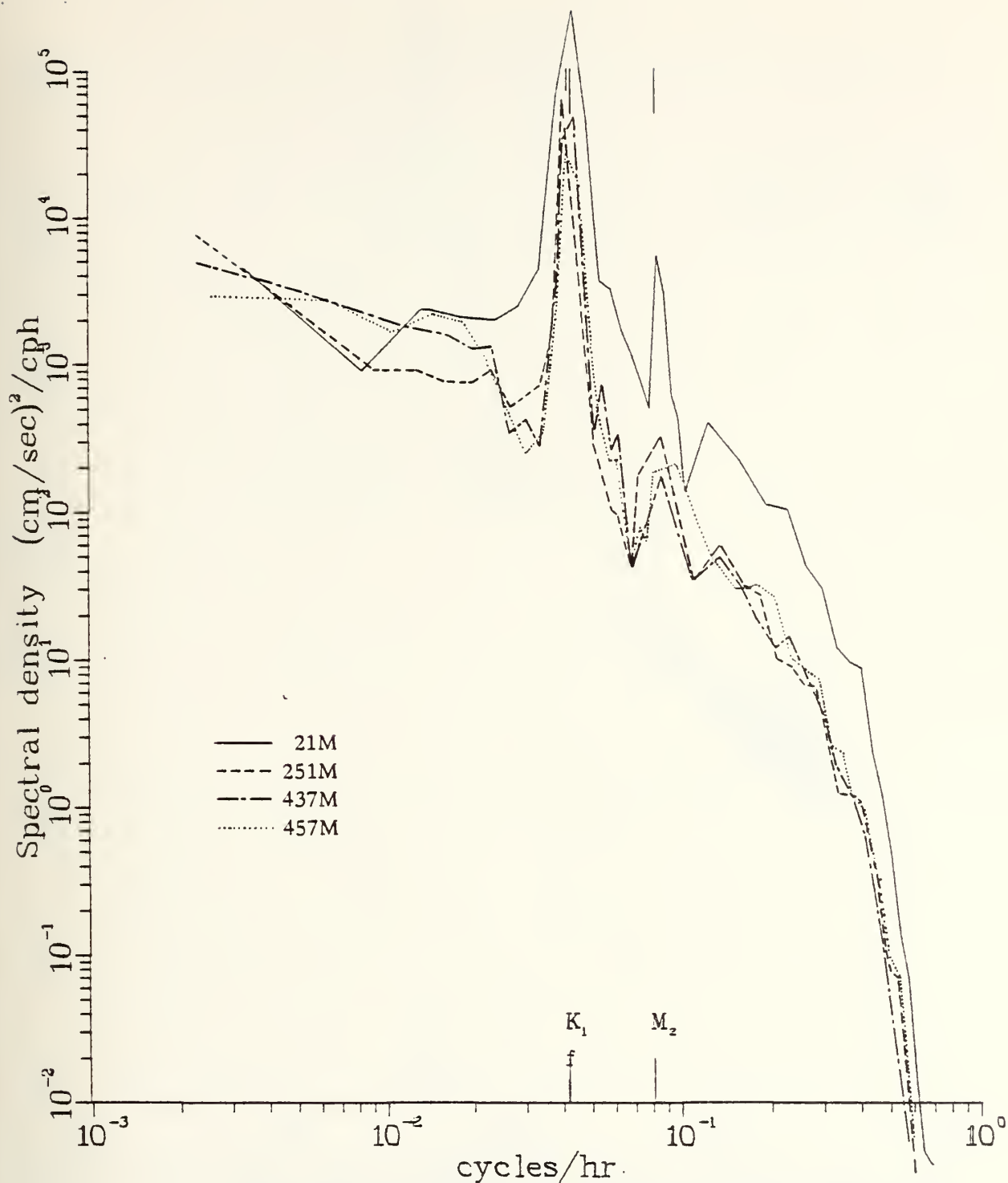


Figure 13. Normalized HKE Spectra from CMA3 at 21 m (solid), 251 m (dashed), 437 m (dashed-dotted) and 457 m (dotted). K₁ represents the diurnal tide frequency, f the inertial frequency and M₂ the semi-diurnal tide frequency.

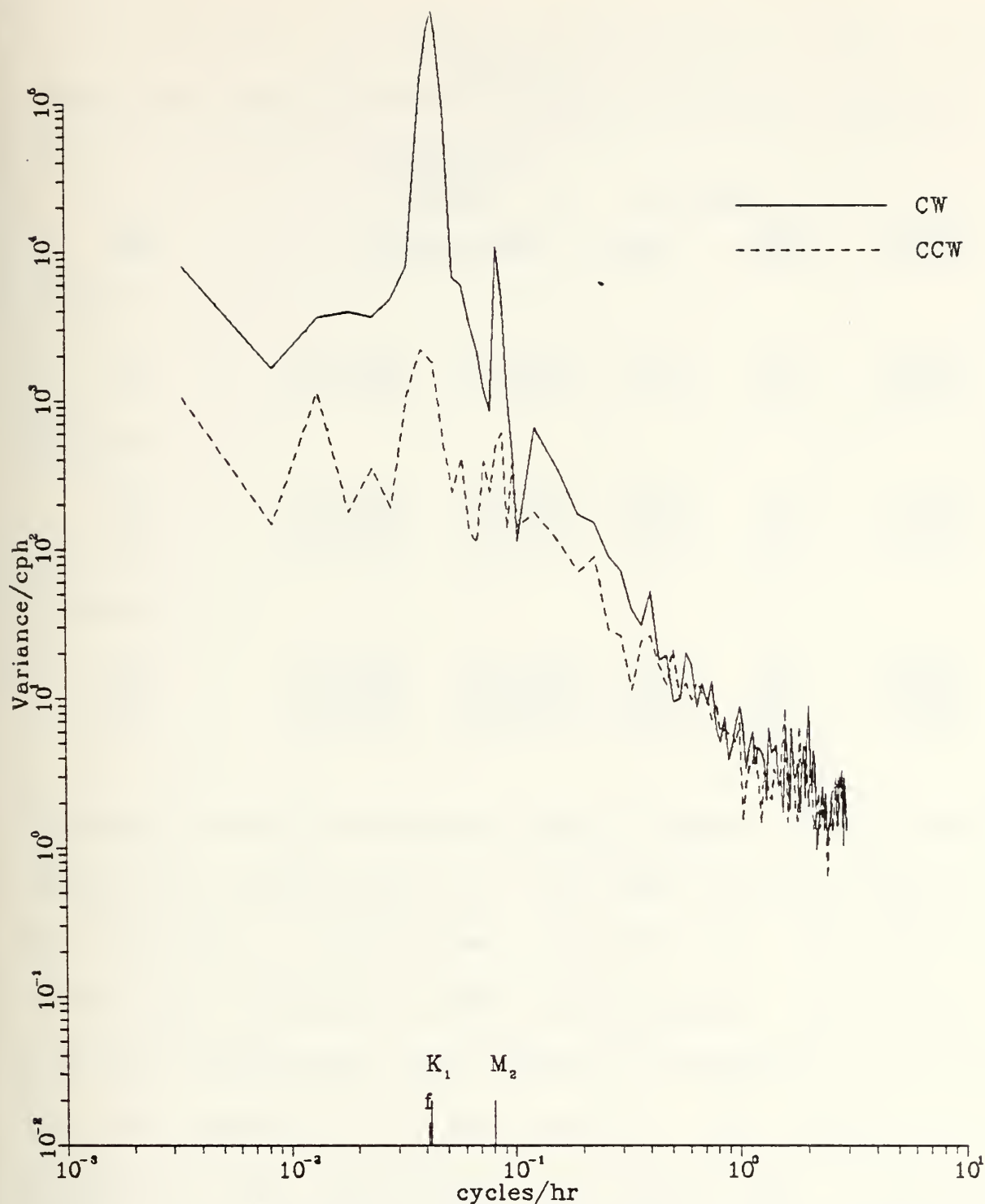


Figure 14. Mixed Layer Normalized Rotary Spectra from CMA3 for CW motion (solid) and CCW motion (dashed). K_1 represents the diurnal tide frequency, f the inertial frequency and M_2 the semi-diurnal tide frequency.

TABLE IV

Normalized Rotary Spectrum Analysis at Inertial Frequency

Depth (m)	Normalized Rotary Spectra		Ellipse		Rotary Coeff.
	CW (cm/s) ² /cph	CCW	Stab.	Dir. (Deg.)	
a) <u>CMA1</u>					
49	6.7x10 ⁺³	1.3x10 ⁺³	0.81	18	+0.68
64	2.5x10 ⁺³	1.4x10 ⁺³	0.20	65	+0.62
b) <u>CMA2</u>					
19	1.8x10 ⁺⁵	3.5x10 ⁺³	0.90	60	+0.96
179	4.6x10 ⁺⁴	3.7x10 ⁺²	0.95	80	+0.95
324	2.8x10 ⁺⁴	1.3x10 ⁺²	0.30	60	+0.96
c) <u>CMA3</u>					
21	4.0x10 ⁺⁵	2.0x10 ⁺³	0.87	50	+0.98
251	1.4x10 ⁺⁵	6.1x10 ⁺²	0.63	90	+0.98
437	1.2x10 ⁺⁵	6.3x10 ⁺²	0.50	150	+0.98
457	6.2x10 ⁺⁴	5.0x10 ⁺²	0.77	160	+1.00

direction of the near-bottom ellipse rotated CCW with depth between the thermocline (179 m) and near the bottom (324 m). The stability of the ellipses indicated that the inertial motion near the bottom at CMA2 was isotropic. In contrast, inertial oscillations were strongly anisotropic at all of the other depths in the deep region. The inertial wave response at CMA1 was markedly less intense than at CMA2 or CMA3, but it was polarized in a CW sense. The reasons for the semi-diurnal tide at CMA1 being much more energetic than the inertial motion is explained below.

The vertical and horizontal coherences are computed to estimate the spatial scales. The spatial scale L is computed from the cross-spectral phase relationship using

$$L = \frac{360}{\Delta\phi} \Delta d \quad (3)$$

where Δd is either the vertical or horizontal distance between the current meters and $\Delta\phi$ is the phase difference between similar velocity components (Pollard, 1980). This analysis is restricted to the CMA2 and 3 due to the absence of an energetic inertial response at CMA1 (Table V). Estimates of vertical scales are more accurate than the horizontal scale estimates because the vertical spacing of the current meters below the mixed layer is not the same at the two arrays. These scales calculated from the entire storm time series will be compared below with the scales calculated from the instantaneous phases.

The vertical cross-spectral analyses (Table V) indicate that the inertial response in the mixed layer led the near-bottom response. The normalized cross-spectrum variance between the vertical levels was about a factor of two greater at CMA3 than at CMA2. The vertical scales computed from (3) are about 360 and 540 m at CMA2,3 respectively.

That is, the inertial motion had scales of the order of the water depths at both arrays and was coherent at the 95 % confidence level.

TABLE V
Vertical and Horizontal Coherencies at the Inertial Frequency

Array	Variables	Normalized Cross-Spectra Variance/cph	Squared Coherence	Phase (deg.)
<u>Vertical</u>				
2	u (s) , u (b)	$3.2 \times 10^{++}$	0.62	-50
2	v (s) , v (b)	$2.7 \times 10^{++}$	0.60+	-70
3	u (s) , u (b)	$6.5 \times 10^{++}$	0.70	-55
3	v (s) , v (b)	$6.0 \times 10^{++}$	0.80	-50
<u>Horizontal</u>				
3,2	u (s)	$1.9 \times 10^{+5}$	0.98	-45
3,2	v (s)	$1.6 \times 10^{+5}$	1.00	-55
3,2	u (b)	$2.3 \times 10^{++}$	0.98	-20
3,2	v (b)	$2.1 \times 10^{++}$	0.95	-30

+ not significant at 95 % confidence

* spectra assumes an average inertial frequency of 0.0412 cph
(s) = surface layer (CMA2 = 19 m ; CMA3 = 21 m)
(b) = bottom layer (CMA2 = 324 m ; CMA3 = 457 m)

The instantaneous phase differences of the velocity components between the two records can also be used to estimate the vertical scales (Fig. 15). Initially, the estimated vertical scales at CMA3 were much greater (typically 800 to 900 m) than the water depth, but after JD 257 the estimates were consistently of the order of the water depth. The

large vertical scales observed initially agree with those estimated from the Eloise simulations by Price (1983) and the Allen observations by Brooks (1983). At CMA2, the vertical scales had similar trends and converge to scales of the order of the water depth.

The horizontal cross-spectrum estimates (Table V) indicate both velocity components were coherent in the mixed layer. The corresponding scales, as estimated from (3), are 20 and 35 km in the east-west and north-south directions using an array separation of 34 km. Initially, the horizontal scales were set by the atmospheric forcing, but these estimates may be somewhat biased because the entire storm time series was used in the computation of the spectra. The cross-spectrum variance between the two near-bottom records was about one order of magnitude less than in the mixed layer. However, these values are significant at the 95 % confidence level as indicated by the coherence squared. The response at CMA2 leads the response at CMA3 by about 2 h. The horizontal scales near the bottom calculated from (3) are 20 and 35 km in the east-west and north-south directions, respectively. The differences in the scales are due to the larger scales set up by the hurricane in the

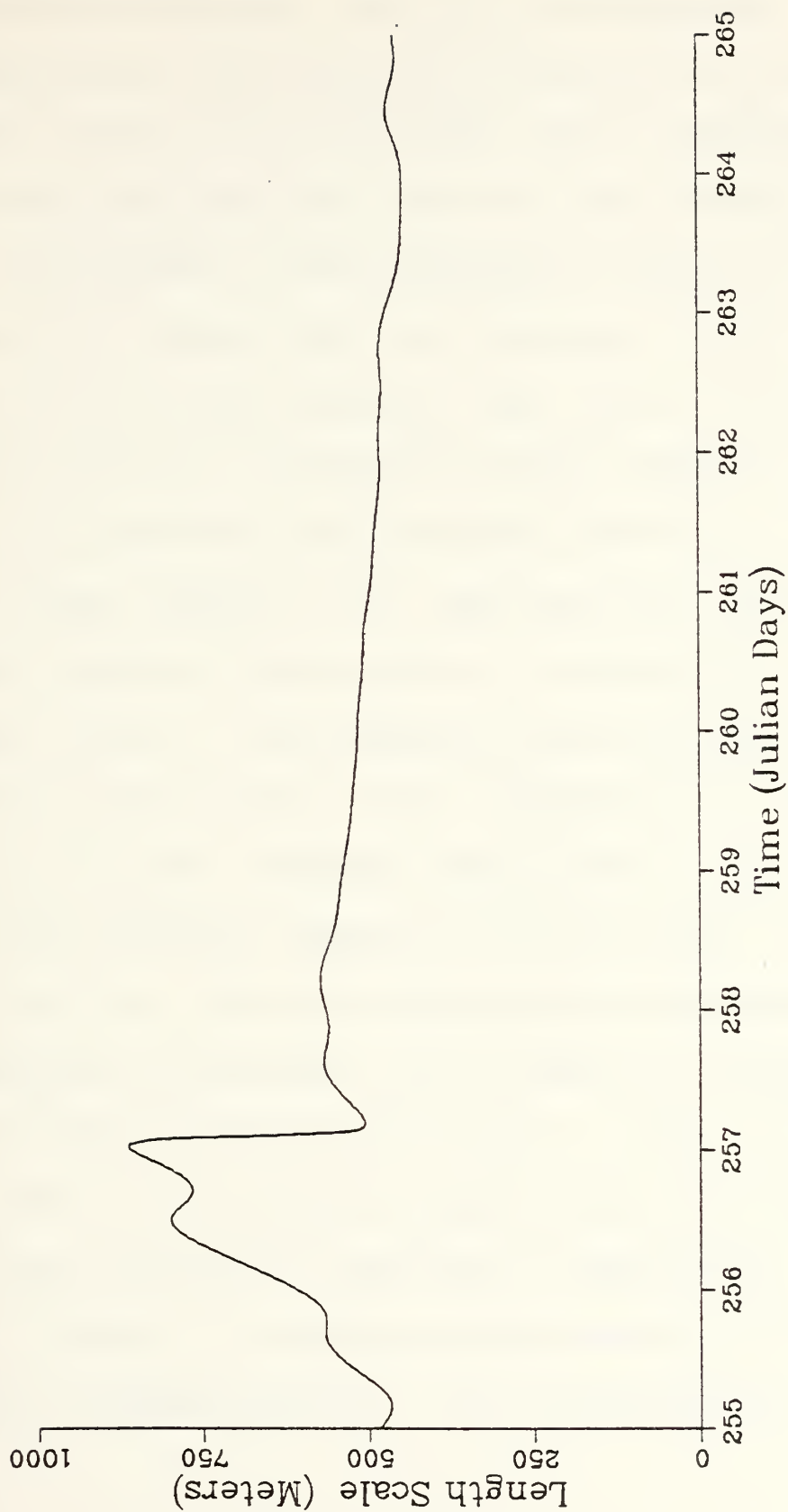


Figure 15. Vertical Scales at CMA3 computed from the instantaneous phase differences between the U velocity components at 21 m and 457 m.

along-track (north-south) than in the cross-track (east-west) directions. These estimates of scales may be somewhat misleading because of the instrument depth difference (135 m), although they agree well with mixed layer estimates.

The instantaneous phase differences between the mixed layer currents indicate that the horizontal length scales were set by the storm initially (Fig. 16). The scales decreased rapidly and approached constant values of 60 and 100 km in the east-west and north-south directions, respectively. These scales in the mixed layer are roughly 1-2 times the baroclinic Rossby radius of deformation for the first mode (56 km). The estimates of the horizontal scales of inertic-gravity waves in the thermocline are computed from the bottom and mid-depth instantaneous phase differences in the U-velocity component at CMA2 and CMA3, respectively (Fig. 17). The east-west and north-south scales in the thermocline immediately after hurricane passage are roughly the same as in the mixed layer. After 4 IP, the scales revert to the pre-storm scales of 25 and 50 km in the east-west and north-south directions, respectively. Some caution is advised in accepting these estimates due to the large depth difference of 73 m. In a later section, it is

suggested that the energy was contained primarily in the barotropic and first two baroclinic modes. Hence, a depth difference of 73 m may be acceptable within the deeper thermocline because of the relatively large displacement of the isotherms, the large vertical scales, and the amount of energy contained in the barotropic mode.

The estimates of vertical energy propagation speed are computed only on the basis of the lag times between the surface and subsurface response (Table VI). In the first case, the response is felt at the bottom of the water column within 3 to 4.5 h after increases in the mixed layer are detected. The initial response corresponds to a vertical scale of roughly 900 m (Fig. 15). This lag of 3 to 4.5 h results in a vertical energy propagation speed of 2.6 km/d which is roughly 1 to 2 orders of magnitude greater than the values calculated by Brooks (1983) and Price (1983). The 10 IP lag in the second maximum observed at 251 m represents a vertical energy propagation speed of 26 m/d when the vertical scale is about 500 m. This vertical propagation of energy agrees quite well with the estimates derived from the Allen observations. However, there is also a second maximum observed near the bottom about 6 IP following the storm.

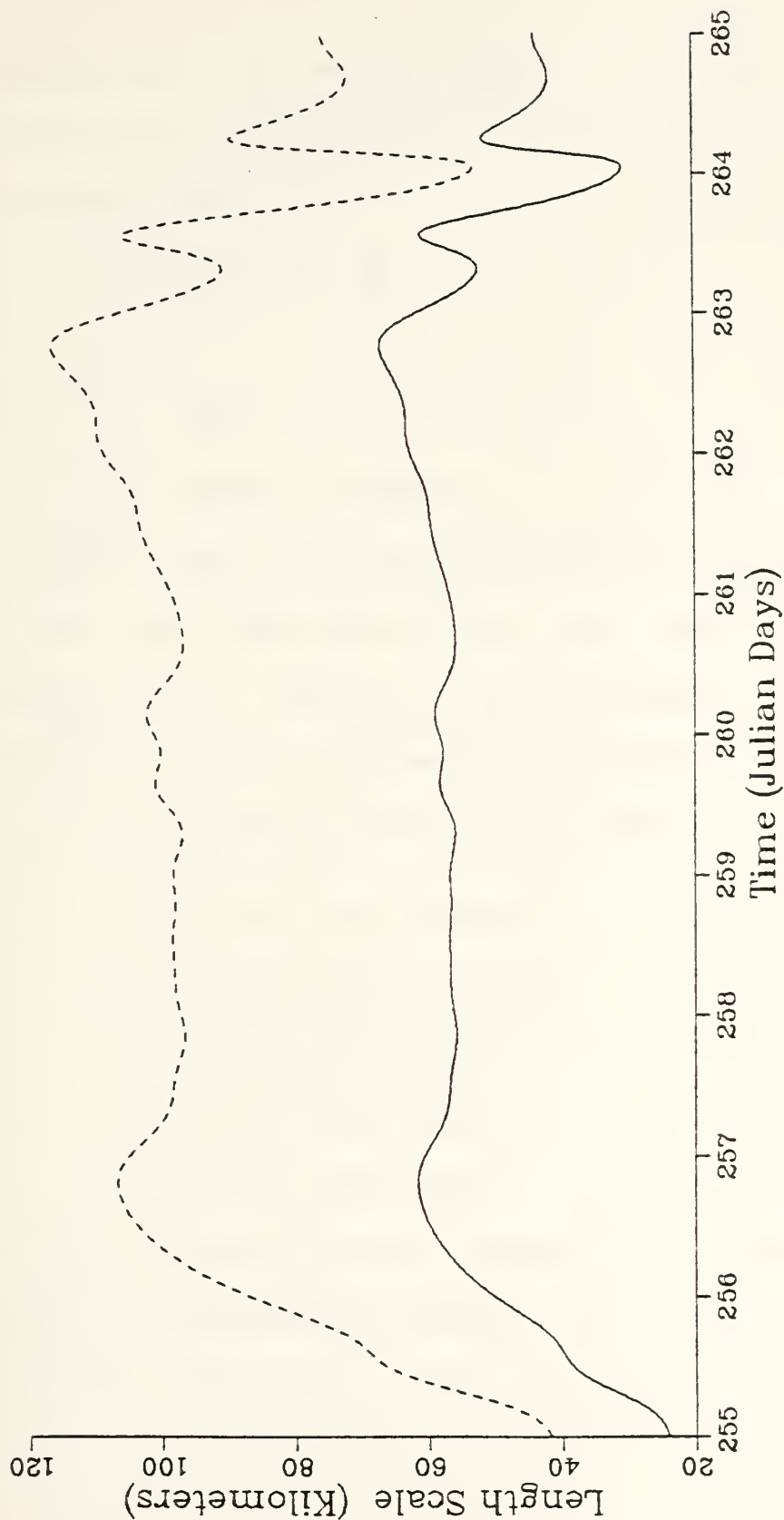


Figure 16. Estimates of Horizontal Scales in the Mixed Layer based on the instantaneous phase differences between the velocity components at CMA2 (19 m) and CMA3 (21 m). The east-west and north-south scales are depicted by solid and dashed curves.

Consequently, the vertical (C_{gz}) and horizontal (C_{gH}) group velocities are calculated from the following expressions (Brooks, 1983)

$$C_{gz} = - \frac{\sigma}{m} \frac{N^2}{\sigma^2} \tan^2 \theta \quad ? \quad (4)$$

$$C_{gH} = \frac{\sigma}{k} \frac{N^2}{\sigma^2} \tan^2 \theta \quad ? \quad (5)$$

where σ is the observed frequency, m and k are wavenumbers in the vertical and horizontal cross-track directions, and $\tan \theta = k/m$. The wavenumbers m and k are equal to $2\pi/L_z$ and $2\pi/L_H$ respectively, where L_z and L_H represent the vertical and horizontal scales as estimated previously. The assigned values to the variables in (4) and (5) are

$$\sigma = 7.54 \times 10^{-5} \text{ rad/s},$$

$$N^2 = 3.30 \times 10^{-5} \text{ rad}^2/\text{s}^2,$$

$$m = 6.98 \times 10^{-3} \text{ rad/m},$$

$$k = 1.16 \times 10^{-2} \text{ rad/m},$$

$$k = 1.05 \times 10^{-4} \text{ rad/m}.$$

The initial vertical group velocity is 1.25 km/d as computed from the dispersion relation (4) with an initial scale of 900 m (Table VI). This estimate is about half of

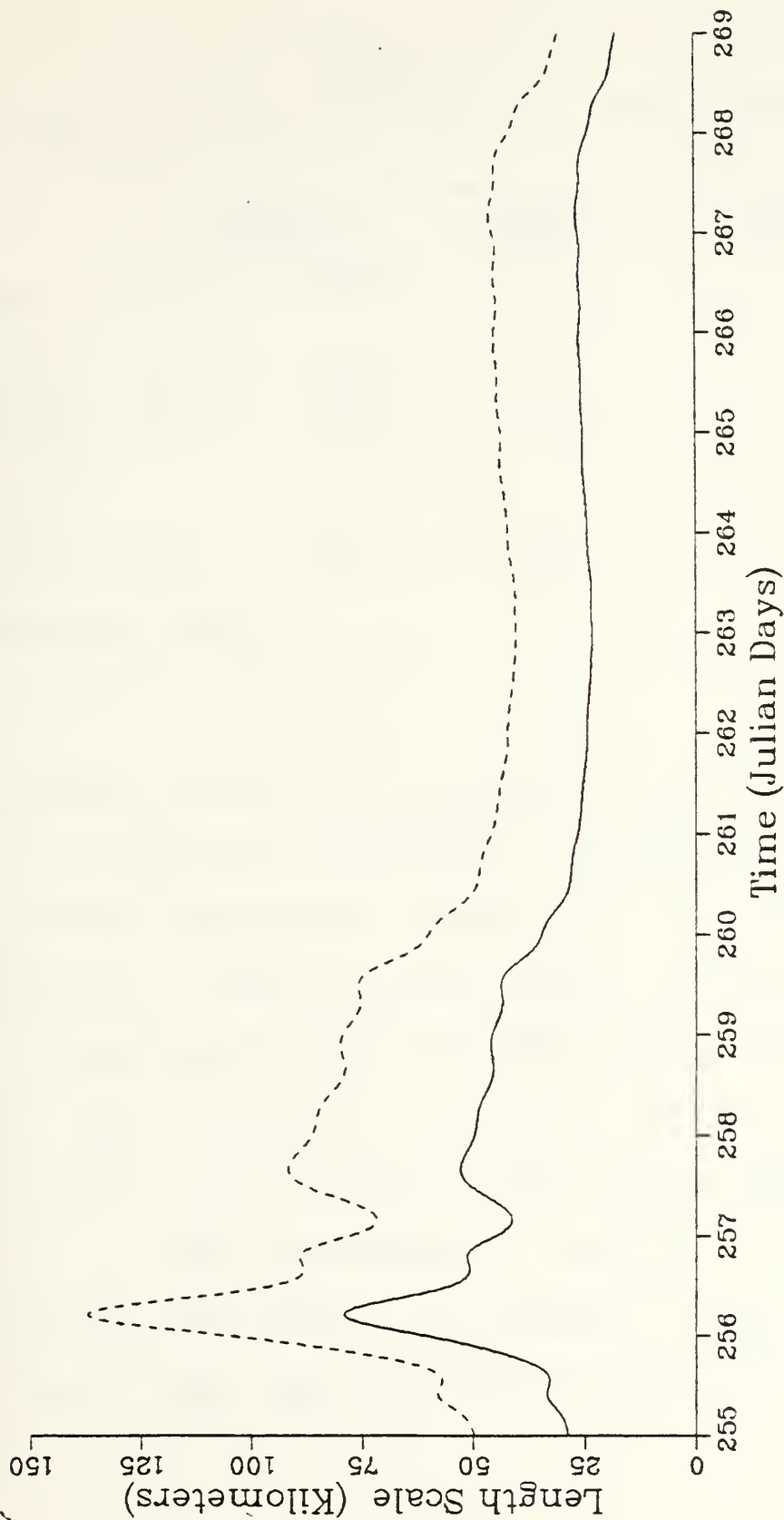


Figure 17. Horizontal Scales in the Deep Thermocline based on the instantaneous phase differences between the velocity components at CMA2 (324 m) and CMA3 (251 m). The east-west and north-south scales are depicted by solid and dashed curves.

TABLE VI

Comparison of Vertical and Horizontal Group Velocity.

	Vertical Scales		Brooks *	Price *
	900 m	500 m		
Vertical Group Velocity				
Lag Time	2.6	0.03		
Dispersion (km/d)	1.3	0.27	.06	.160
Horizontal Group Velocity				
Dispersion (km/d)	80.	30.	23.	86.
* From Brooks (1983)				

the one computed based on the initial lag time and is still an order of magnitude larger than the estimates computed from the Eloise simulations. After a few IP, the vertical group velocity is about 0.27 km/d, which is of the order of the Eloise estimates of about 0.16 km/d (Price, 1983). Furthermore, this estimate is about one order of magnitude larger than the value of 0.02 km/d that Brooks (1983) estimated from the Allen observations. Clearly, the initial storm forcing causes energy to propagate vertically at a significantly higher rate than after a few IP following the storm.

The horizontal propagation of energy is a much more rapid than the vertical propagation (Table VI). The group velocity estimate for the Frederic observations is initially 80 km/d; and it decreases to about 30 km/d a few IP following the storm. This difference is due to the \tan^2 dependence on m as previously defined. The initial horizontal group velocity estimate agrees with the Price (1983) estimate whereas the lower value agrees with the Brooks (1983) estimate. The horizontal phase speeds of the inertio-gravity waves in the wake of Frederic are about 70 cm/s with a vertical phase speed of roughly 1 cm/s.

In summary, inertial waves maintained a constant amplitude over 1 to 2 IP following the passage of Frederic. These oscillations in the mixed layer then relaxed over an e-folding scale of about 4 IP. In the subsurface layers, the forced inertio-gravity waves decayed over similar time scales after the appearance of a secondary maximum. The lag between the initial impulse of energy and the second subsurface maximum varied over depth. For example, this period was about 10 IP at 251 m, but it was only 6 IP at 457 m. These lag values define a modulation envelope which evolves in time. If vertical propagation of energy from the mixed

layer alone accounts for these secondary maxima, why do the maxima occur later in the deep thermocline than near the bottom ? Other mechanisms besides dispersion of energy from the mixed layer must be responsible. For example, nonlinear resonant interactions among the inertio-gravity waves could be responsible (McComas and Bretherton , 1977). Analyses of these interactions are beyond the scope of the present work.

The initial vertical scales of the inertio-gravity waves in the wake of Frederic are approximately equal to the Eloise and Allen estimates. However, after a few IP the vertical scale decreased to about 500 m or approximately the water depth. The horizontal scales estimated from the Frederic observations differ greatly from the Allen data and Eloise simulations. The horizontal scales during Allen were four times the mixed layer horizontal scales observed immediately after the passage of Frederic. This difference increased to a factor of about eight approximately 4 IP after Frederic. These discrepancies may be due to the rugged bottom topography in the DeSoto Canyon region.

B. SUBINERTIAL RESPONSE

The forcing by hurricane Frederic also altered the "mean flow" and the lower frequency motions (periods greater than

3 IP). The variability and response of the mean flow to the forcing is depicted in progressive vector diagrams (PVD). The ocean current data were low-pass filtered with a half power point at 26 h to isolate the forced response on the lower frequency variability.

The mean flow in the mixed layer at CMA2 was directed towards the east prior to the storm (Fig. 18a). During the passage of hurricane Frederic near JD 256, there was only a small deflection in the mean flow. The subsequent horizontal displacements indicate that the mean flow was about 26 km/d, or almost twice the mean current during the pre-storm period. The mean flow at 179 m (not shown) at CMA2 also increased towards the east.

The bottom PVD at CMA2 indicates that the mean flow at that level was more or less constant (Fig. 18b). However, the direction of this flow was opposite to that observed in the mixed layer. Consequently, the bottom PVD was nearly a mirror image of the surface PVD, although the bottom flow was slower than that of the mixed layer. There was also a superposed lower frequency motion of about 3 IP near the bottom, particularly during the period between the initial and secondary maxima of HKE (first 6 IP in Fig. 9). The

lower frequency oscillations may be due to coastally trapped waves, which were enhanced by the storm, since waves of the same period were observed during the quiescent period (Appendix E). These waves can be altered by both bottom topography and continuous density stratification (Wang and Mooers, 1976). A study of the mechanisms by which the mean flow is altered by these waves and the rugged terrain is also beyond the scope of this thesis.

At CMA3, the surface mean flow was southward prior to the storm (Fig. 19a). At the time of storm passage, near JD 256, the surface mean flow was deflected outward from the storm center. Between JD 257 to 269, the mean flow accelerated to about 13 km/d and then decelerated to about 6 km/d towards the south. Prior to the storm, the mean flow near the bottom at CMA3 was northward following the local bottom topography (Fig. 19b). There was an eastward (up the canyon slope) deflection late on JD 256. After completing a loop, the mean flow veered towards the northwest (down the canyon slope). Between JD 254 to 263, the mean flow near the bottom was considerably faster than either earlier or later times. Again, the mean flow near the bottom was reversed relative to that in the mixed layer.

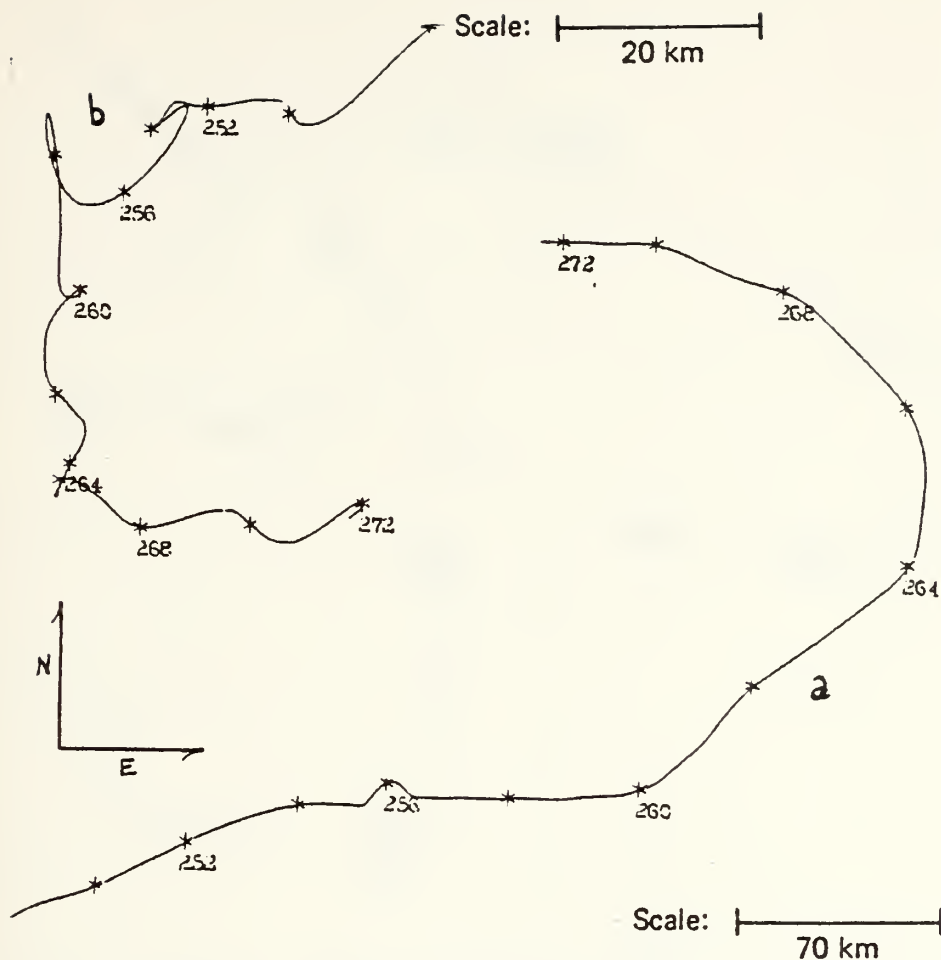


Figure 18. Low-pass Filtered PVD at CMA2. The * represents a time interval of 48 h starting on JD 248 for a) mixed layer (19 m) and b) bottom Layer (324 m).

Thermocline temperatures in the wake of Frederic varied spatially as well temporally. There were sizeable subinertial oscillations as well as near-inertial oscillations in the temperature signal (Fig. 20). These temperature variations were typically 3.0°C at both array sites and were superposed on mean temperatures that range between 13.0 to

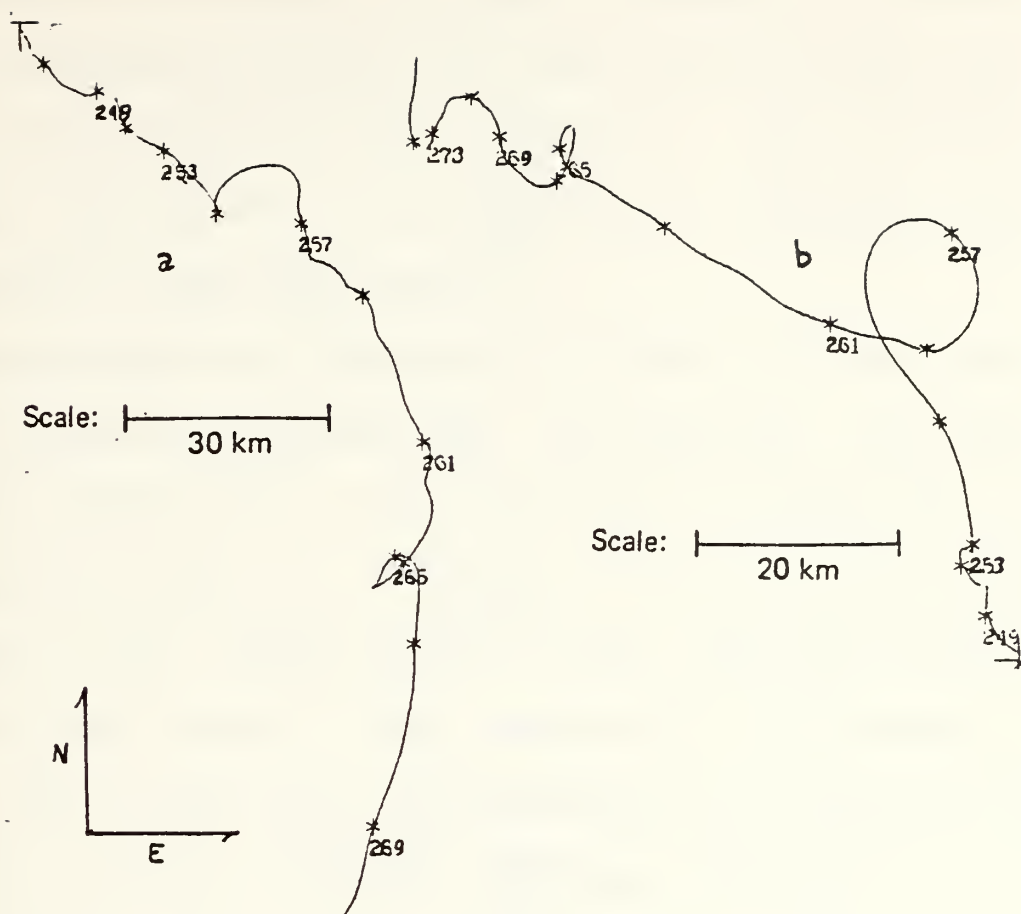


Figure 19. Low-pass Filtered PVD at CMA3. The * represents a time interval of 48 h starting on JD 245 for a) mixed layer (21 m) and b) bottom Layer (457 m).

14.5°C in the thermocline. At CMA3, the temperature at 251 m started to increase about 0600 GMT on JD 255 and continued to increase over the next 15 h due to the strong northward current. The temperatures then decreased by 2°C due to a strong southward current. Inertial fluctuations of about 3°C persisted over the subsequent 8 IP. After this time,

the variations underwent a slight increase in frequency which corresponded to about the time of the secondary maximum in the horizontal velocity components. For the remainder of the record, the temperature variations were superposed on a stationary mean.

Bottom temperature variability at CMA2 is a clear example of advective processes that are associated with lower frequency motions (Fig. 21). On JD 254 (11 September), a temperature decrease of 1.30°C over a 16 h period marked the beginning of the forcing period as cool water was advected from the DeSoto Canyon. The temperature then increased by 3.70°C over the next 25 h as warm water was advected by the southward velocity component which was downslope in this part of the canyon. As the winds relaxed, cooler water was again advected into the area. Around JD 260, the temperature dropped by 4°C over an 11 hour period. This drastic change in temperature was due to the advection of cold water by these subinertial waves of 3 IP period. From the orientation of the ellipses (Table VII), the direction of the wave propagation was northward (upslope, away from the DeSoto Canyon). These waves set up cross-shelf oscillations (relative to CMA2) in the north-south direction. After

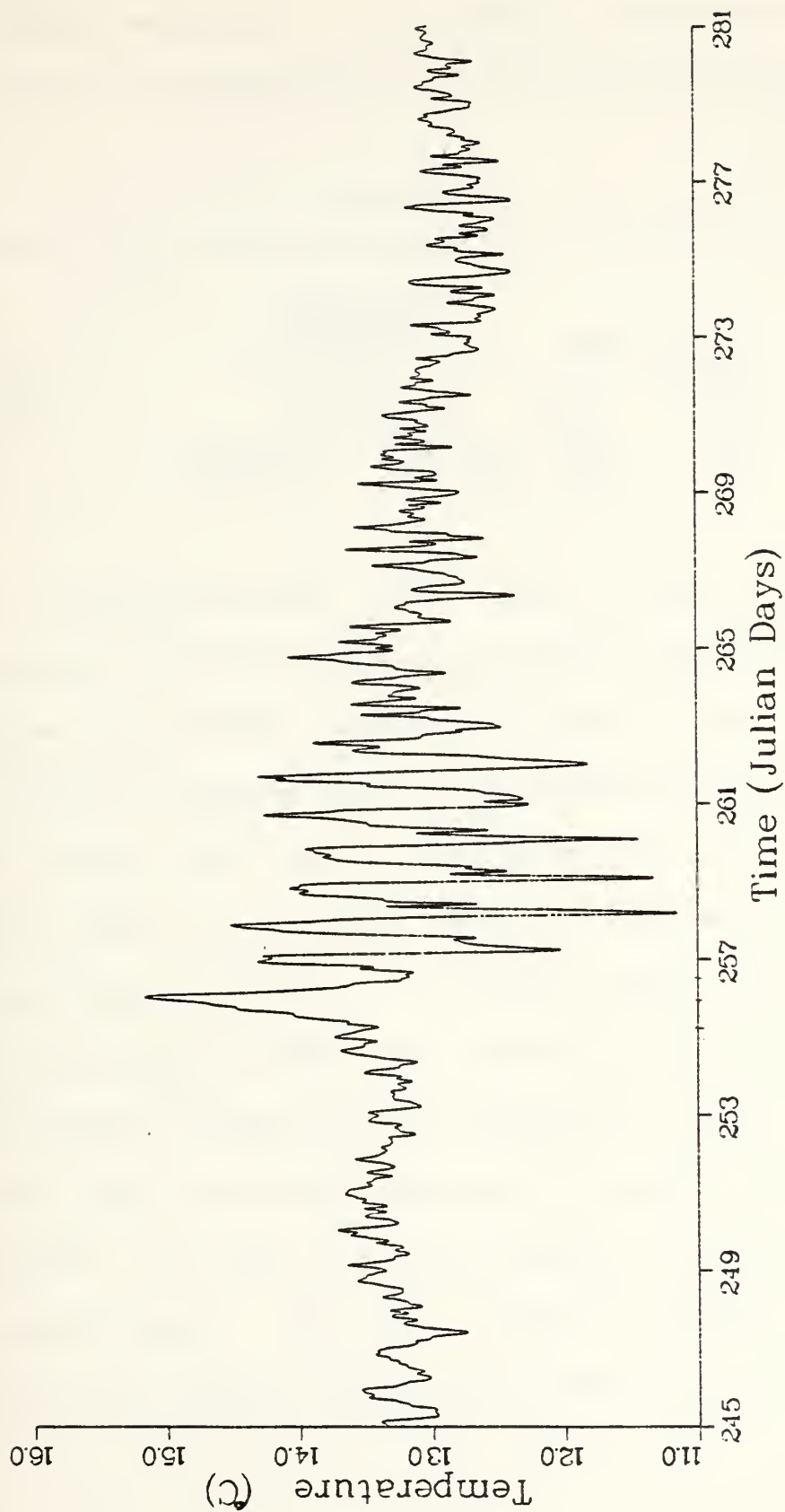


Figure 20. Thermocline Temperature Time Series from CMA3 at 251 m.

these large variations, near-inertial oscillations in the temperature were superposed on a gradual warming trend.

TABLE VII

Normalized Rotary Spectrum Analysis at Subinertial Frequency

Depth (m)	Normalized Rotary Spectra		Ellipse		Rotary Coeff.
	CW (cm/s) ² /cph	CCW	Stab.	Dir. (Deg.)	
324	4.5x10 ⁺³	3.0x10 ⁺³	0.65	10	+0.20
457	4.7x10 ⁺³	1.0x10 ⁺²	0.50	10	+0.98

The potential energy spectra were computed using the temperature time series and the vertical temperature gradients from the AXBT data collected by Black (1983) (Appendix A). The most prominent peak in the potential energy spectra at CMA3 is near the inertial frequency (Fig. 22). The most energetic peaks at the semi-diurnal and subinertial frequencies are near the bottom. Potential energy variability in the bottom layers at CMA2 (not shown) is significant at the 95 % confidence levels only for periods of about 3 IP.

From rotary spectrum analyses at periods of 3 IP near the bottom: (1) the CW and CCW rotating components at CMA2 were nearly equal, with just a slight tendency towards CW polarization; and (2) the motion at CMA3 was polarized in a

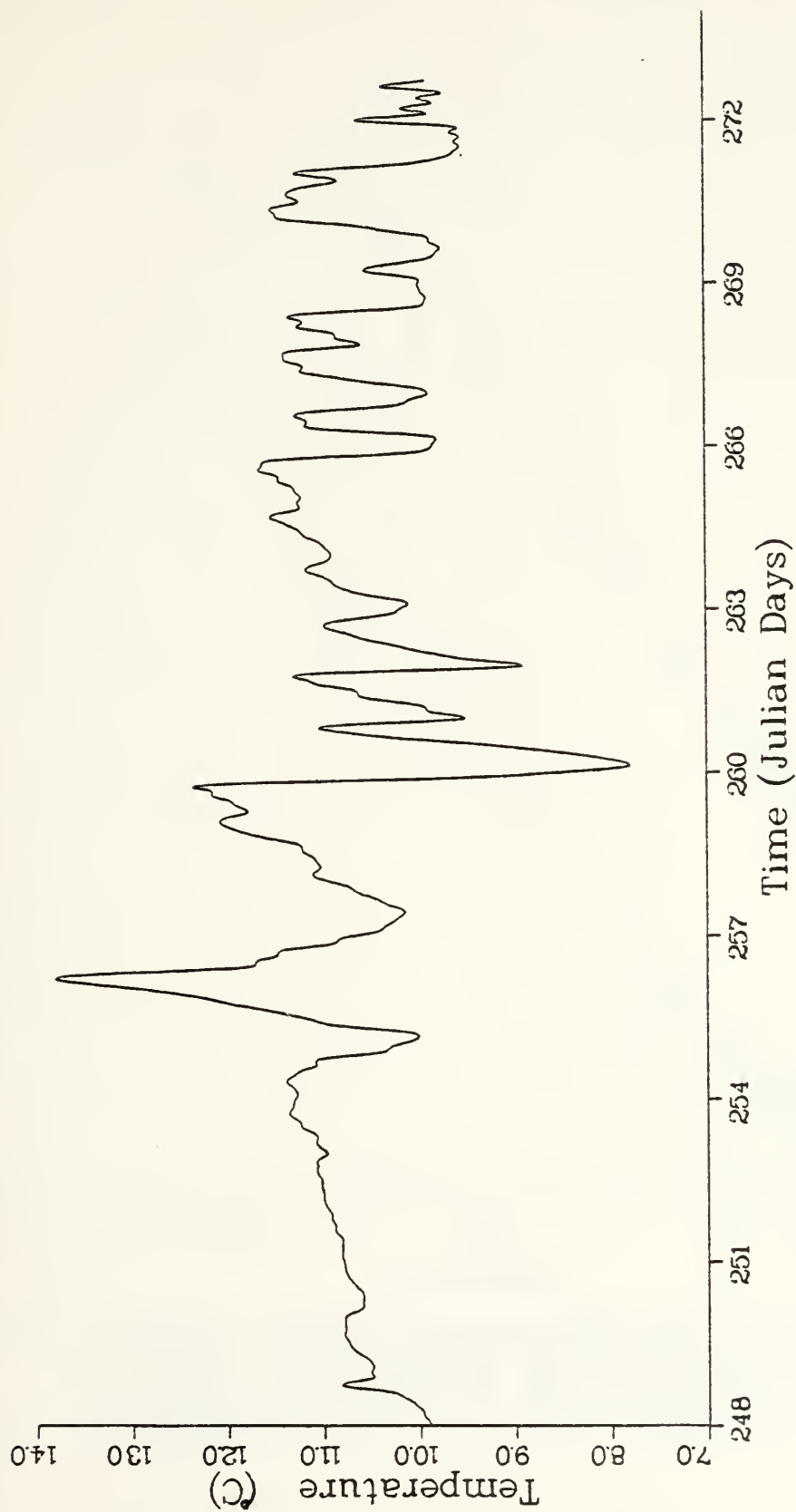


Figure 21. Temperature Time Series from CMA2 at 324 m.

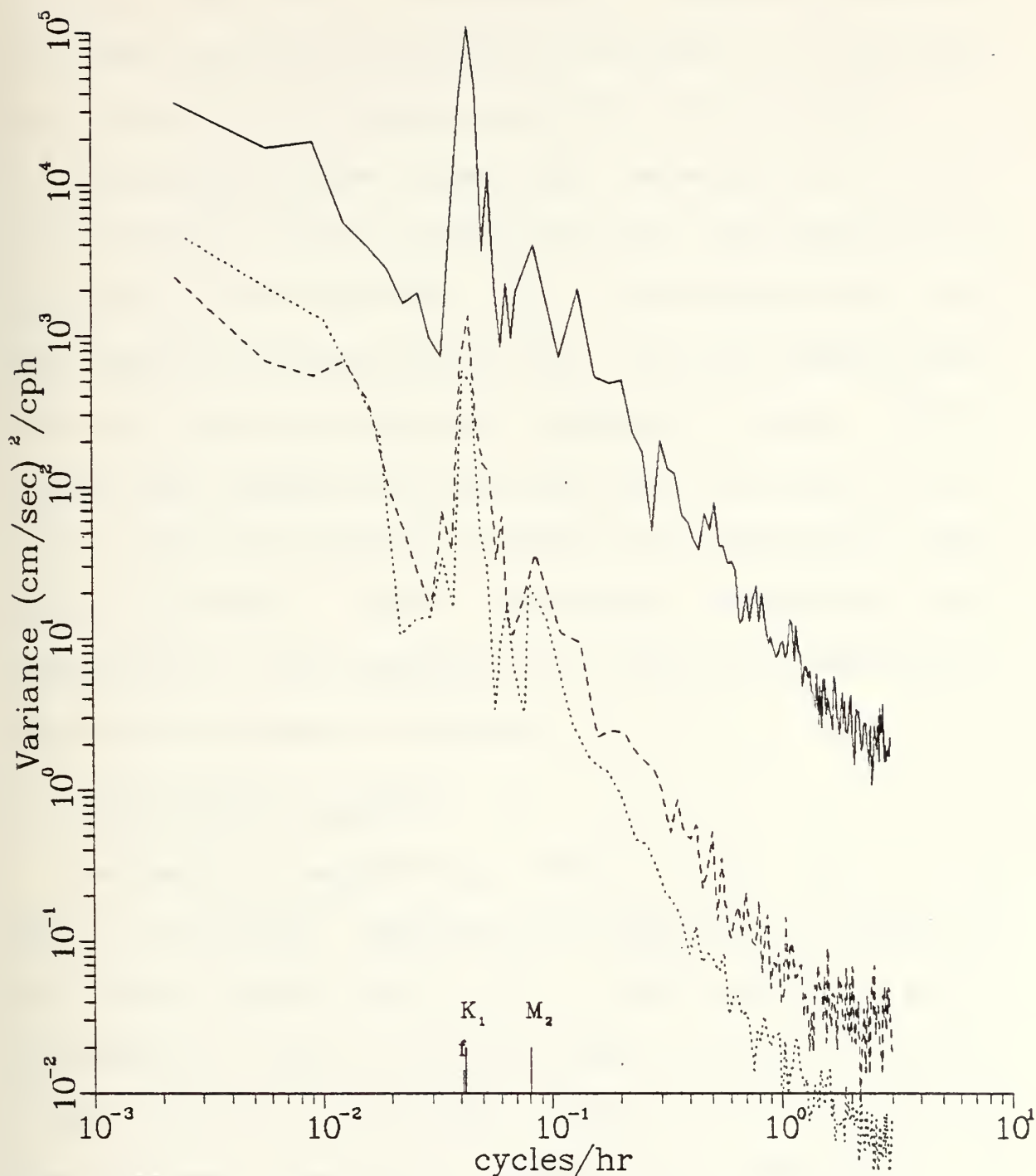


Figure 22. Potential Energy Spectra from CMA3 for the isotherm displacements observed at 251 m (solid), 437 m (dashed) and 457 m (dotted). K_1 represents the diurnal tide frequency, f the inertial frequency and M_2 the semi-diurnal tide frequency.

CW sense (Table VII). Furthermore, the phase propagation for these longer period waves was northward, and anisotropic as indicated by the ellipse orientation and stability.

The cross-spectrum between the temperature and north-south velocity records at the bottom was also dominated by the peak at about 3 IP (Fig. 23). The corresponding phase and coherence estimates are 100 deg. and 0.98 respectively, with the velocity leading the temperature signal. Hence, these lower frequency oscillations in the cross-shelf direction at CMA2 were properly oriented for advecting the temperature pattern. These cross-shelf oscillations were responsible for the variability in the bottom temperature 4 IP after the passage of Frederic.

C. SUPERINERTIAL RESPONSE

As Frederic passed within 130 km to the west of the CMA1, the dominant response was a significant increase in the westward current (Fig. 24). This increase was due to convergence of flow on the right side of the storm. By contrast, there was a divergence of flow on the left side of the hurricane, where water was transported off-shelf by the winds. For example, a negative tide was recorded at Biloxi, Mississippi which was indicative of the left side of the

storm. The north-south current only increased by about 20 cm/s, whereas the east-west current increased to 80 cm/s. After the hurricane passage, near-inertial waves persisted over the subsequent 3 IP. The post-storm semi-diurnal tidal currents were more energetic than during the quiescent period and were superposed on a non-stationary trend. At the intermediate depth at CMA1, the current speed increased to 80 cm/s during the period of strong forcing, as the semi-diurnal tidal currents were enhanced.

The presence of internal tides at the semi-diurnal frequency is indicated by the HKE spectra during the storm period at CMA1 (Table VIII). The spectral estimates in the semi-diurnal frequency band are almost equal to the inertial period estimates. Baines (1973) shows that one necessary condition for the presence of internal tides is a marked increase in the semi-diurnal tidal currents. The observed increase in the semi-diurnal tidal currents should be equal to or greater than the inertial effects. The storm-spectral estimates at the semi-diurnal frequency exceed those from the quiescent period by more than order of magnitude (Appendix B). A barotropic tide propagating over the shelf break generates internal tides of semi-diurnal tidal period

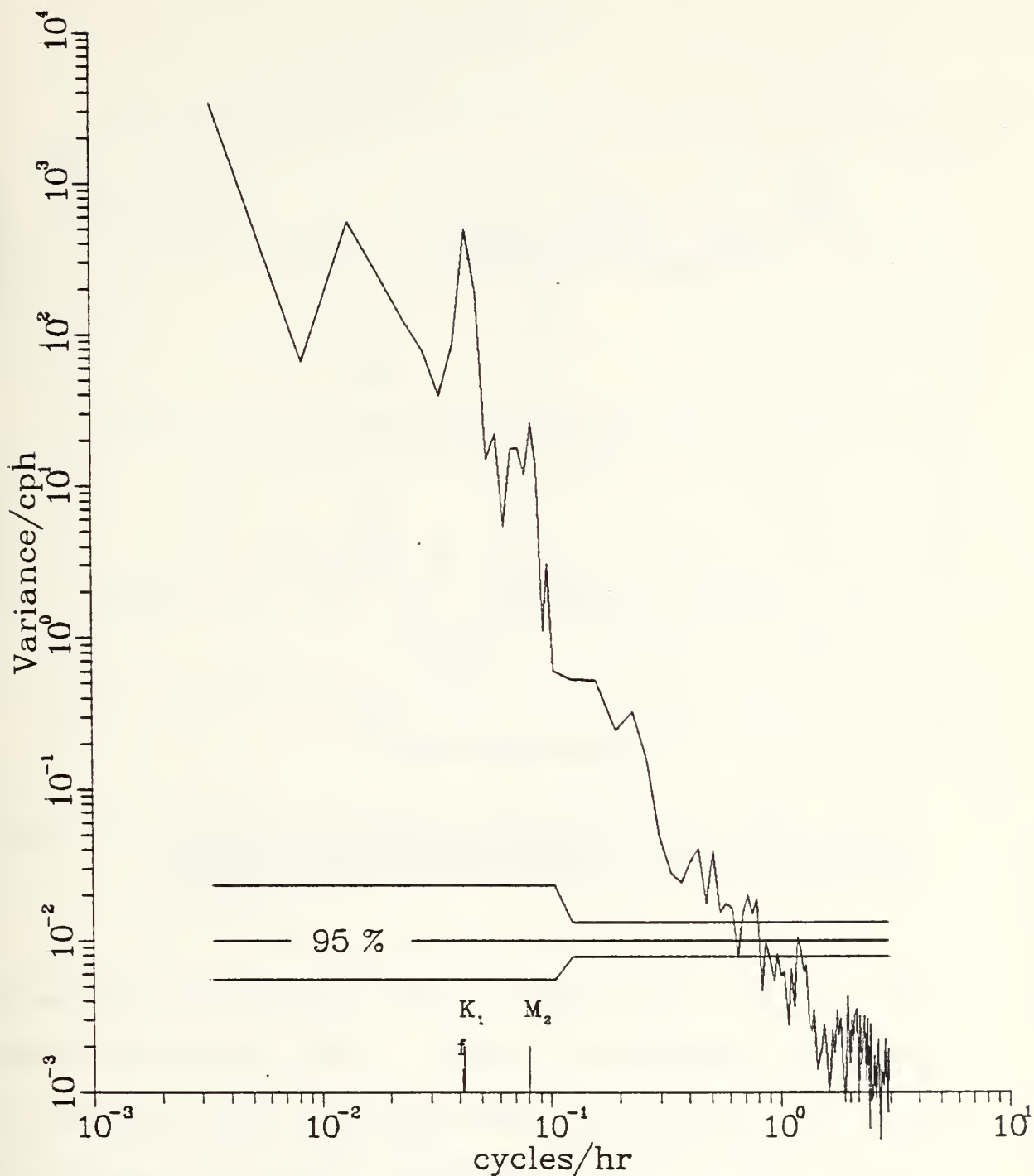


Figure 23. Cross-Spectrum Between V-Velocity and Temperature from CMA2 at 324 m. K_1 represents the diurnal tide frequency, f the inertial frequency and M_2 the semi-diurnal tide frequency.

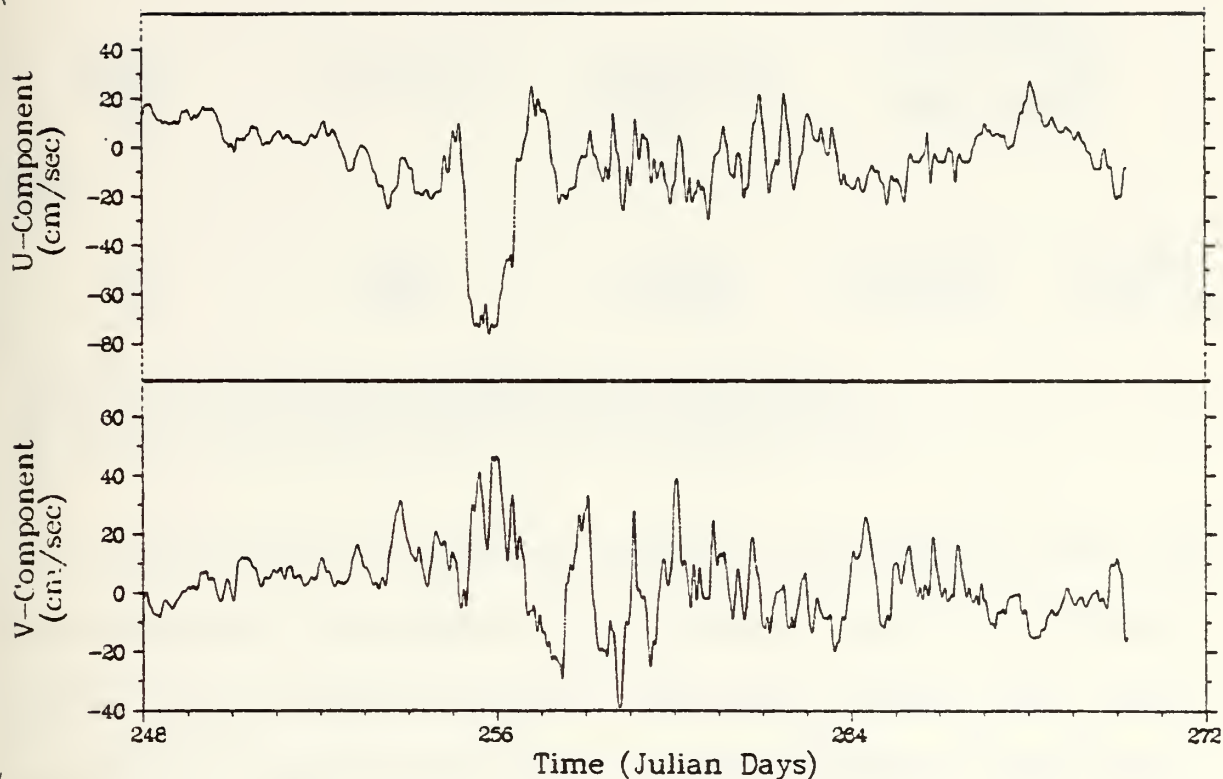


Figure 24. Mid-depth Velocity Components from CMA1. The ordinate depicts magnitude in cm/s of the east-west currents (upper) and north-south currents (lower).

(Prinsenberg and Rattray, 1975 ; Barbee et al., 1975 ; Torgimson and Hickey, 1979). Hence, an increased barotropic tide associated with the storm surge propagating over rugged bottom topography should enhance the internal tides as manifested in the semi-diurnal tidal currents.

TABLE VIII

Normalized HKE Spectra at Inertial and Semi-diurnal Frequency

Meter Depth (<u>m</u>)	No. of Data Points	Frequency Resclution (<u>cph</u>)	Normalized HKE Spectra f M2 (<u>cm/s</u>) <u>2/cph</u>	
<u>CMA1</u>				
49	3200	0.0018	2.0x10 ⁺³	1.0x10 ⁺³
64	2410	0.0025	3.0x10 ⁺³	6.0x10 ⁺²
92*	3000	0.0020	1.4x10 ⁺³	3.2x10 ⁺³

* instrumentation problems with time clock

M2 is the semi-diurnal tide frequency band

f is the inertial/diurnal tide frequency band

The dominance of internal tides on the shelf at CMA1 can be explained by considering the bottom slope in the region. If the bottom slope is greater than the internal wave characteristic, then the rays will not be admitted to the shelf, but instead will be reflected into the oceans interior (Barbee et al, 1975 ; LeBlond and Mysak, 1978 ; Torgrimson and Hickey, 1979). The critical slope for the internal wave characteristic is given by:

$$\frac{dz}{dy} = \left(\frac{\sigma^2 - f^2}{N^2 - \sigma^2} \right)^{1/2} \quad (6)$$

where f is the local Coriolis parameter, which is equal to 7.18 x 10⁻⁵ rad/s near the DeSoto Canyon. The remainder of

the variables have been defined above. The slope of the inertio-gravity wave characteristic is about 4×10^{-3} , whereas in the direction of the canyon axis (45 deg.) the bottom slope is 6×10^{-3} . Therefore, it is clear that the inertio-gravity waves will be reflected seaward as the slope of the characteristic is less than the bottom slope in the DeSoto Canyon region. Inertial oscillations will be locally generated on the shelf but they will only persist for a few IP following the storm. The internal tides, however, will be admitted to the shelf region because the slope of the semi-diurnal tide characteristic is 2×10^{-2} , which is almost an order of magnitude larger than the bottom slope.

The semi-diurnal tides were also enhanced at CMA2 and 3, but they were much less energetic than the inertial waves (Table IX). The CW polarized, semi-diurnal tidal variability was more than an order of magnitude greater than the CCW variability estimates, except in the bottom layers at CMA3. The directions of the semi-major axes of these waves changed from 120 to 20 deg. with depth at CMA2, whereas the opposite occurred at CMA3, where the direction changed from 30 to 50 deg. Hence, the waves were anisotropic and exhibited a strong north-south component of flow at CMA2 and to the northeast at CMA3.

TABLE IX

Normalized Rotary Spectra at the Semi-diurnal Frequency.

Depth (m)	Normalized Rotary Spectra		Ellipse Stab.	Dir. (Deg.)	Rotary Coeff.
	CW (cm/s) ² /cph	CCW			
a) <u>CMA2</u>					
19	1.3x10 ⁺³	4.3x10 ⁺²	0.80	120	+0.30
179	5.0x10 ⁺²	9.0x10 ⁺¹	0.73	60	+0.72
324	4.3x10 ⁺²	1.2x10 ⁺²	0.87	20	+0.41
b) <u>CMA3</u>					
21	1.0x10 ⁺⁴	5.5x10 ⁺²	0.58	30	+0.55
251	6.7x10 ⁺²	1.0x10 ⁺²	0.92	90	+0.70
437	3.2x10 ⁺²	1.3x10 ⁺²	0.40	40	+0.40
457	2.0x10 ⁺²	1.8x10 ⁺²	0.15	50	+0.04

In summary, the superinertial response in the wake of Frederic was dominated by the enhanced semi-diurnal tidal current at all three arrays. The semi-diurnal tidal currents were markedly more energetic than the inertial currents on the continental shelf at CMA1, and agrees with internal tide theory (Baines, 1973). The storm surge, which is associated with the passage of the storm, increases the barotropic tide. As this increased barotropic tide propagates over rugged bottom terrain in a stratified ocean, the increase in the semi-diurnal tidal currents are manifestations of internal tides (Barbee et al, 1975 ; Prinsenberg and Rattray, 1975 ; Torgrimson and Hickey , 1979). Internal

tides can propagate freely up the continental slope and onto the shelf, whereas inertio-gravity waves generated off the slope are reflected towards the interior of the ocean. The rotational characteristics of the semi-diurnal tides, as well as the direction of phase propagation of these waves, are consistent with these theories.

V. NORMAL MODES

A. THEORY

The Sturm-Liouville problem is solved using the vertical profile of Brunt-Vaisala frequencies and linear wave theory. The vertical eigenvalues of the horizontal velocity are then used to obtain a least squares fit to the Fourier coefficient time series computed from the demodulation of the current meter records. The amount of variability associated with each mode is determined to assist in understanding the modal structure of the inertio-gravity wave response generated by the passage of a hurricane.

The problem is formulated by following the work of Fjeldstad (1958) and making the following assumptions:

- f plane;
- continuous stratification;
- hydrostatic balance with basic state at rest;
- incompressible;
- inviscid; and
- flat bottom.

The governing vertical structure equation for linear, inertio-gravity waves is given by

$$\frac{d^2 W}{dz^2} + \mu^2 \Phi(z) W = 0 \quad , \quad (7)$$

where $W(z)$ gives the vertical structure of the inertio-gravity wave, $\mu^2 = K^2 / \sigma^2 - f^2$, $\Phi(z) = N^2 - \sigma^2$, and $K^2 = k^2 + l^2$, and k and l are the horizontal wave number vectors in the x and y directions, respectively. Furthermore, equation (7) is a second order, homogeneous, ordinary differential equation. The specification of the problem is completed by imposing the following boundary conditions:

$$\frac{dW}{dz} - g\mu W = 0 \quad z=0 \quad , \quad (8)$$

$$W = 0 \quad z=-d \quad . \quad (9)$$

The surface boundary condition (8) is a dynamic boundary condition which states that at the sea surface pressure is continuous across the interface. Boundary condition (9) specifies no normal flow through the bottom. The solution to equations (7-9), which define a well known Sturm-Liouville problem, yields the structure of the vertical velocity for constant N , and, is given by

$$W_n(z) \sim \sin\left(\frac{n\pi z}{d}\right) \quad , \quad (10)$$

where the mode number $n=0,1,2,\dots$. The horizontal velocity eigenfunctions $U(z)$ are given by

$$U_n(z) \sim \cos\left(\frac{n\pi z}{d}\right) \quad ? \quad (11)$$

which is the vertical derivative of $W_n(z)$.

The Sturm-Liouville problem is solved numerically by the predictor-corrector fourth-order method modified by Hamming (Gerald, 1980). This method computes a new vector from four preceding values. A fourth-order Runge-Kutta method is used for the adjustment of the initial vertical increments and the computations of starting values.

The resulting amplitudes of the horizontal velocity eigenfunctions for modes 0 through 3 are shown in Fig. 25. The number of zero crossings equals the mode number. Most of the vertical structure lies in the upper thermocline region near the base of the mixed layer.

B. DATA ANALYSIS

The horizontal eigenfunctions are then fitted in a least squares sense to the time-varying amplitudes of the horizontal velocities. The mathematical details are given in Appendix A with the final matrix equations (16-18). The time evolution of the north-south velocity coefficients at

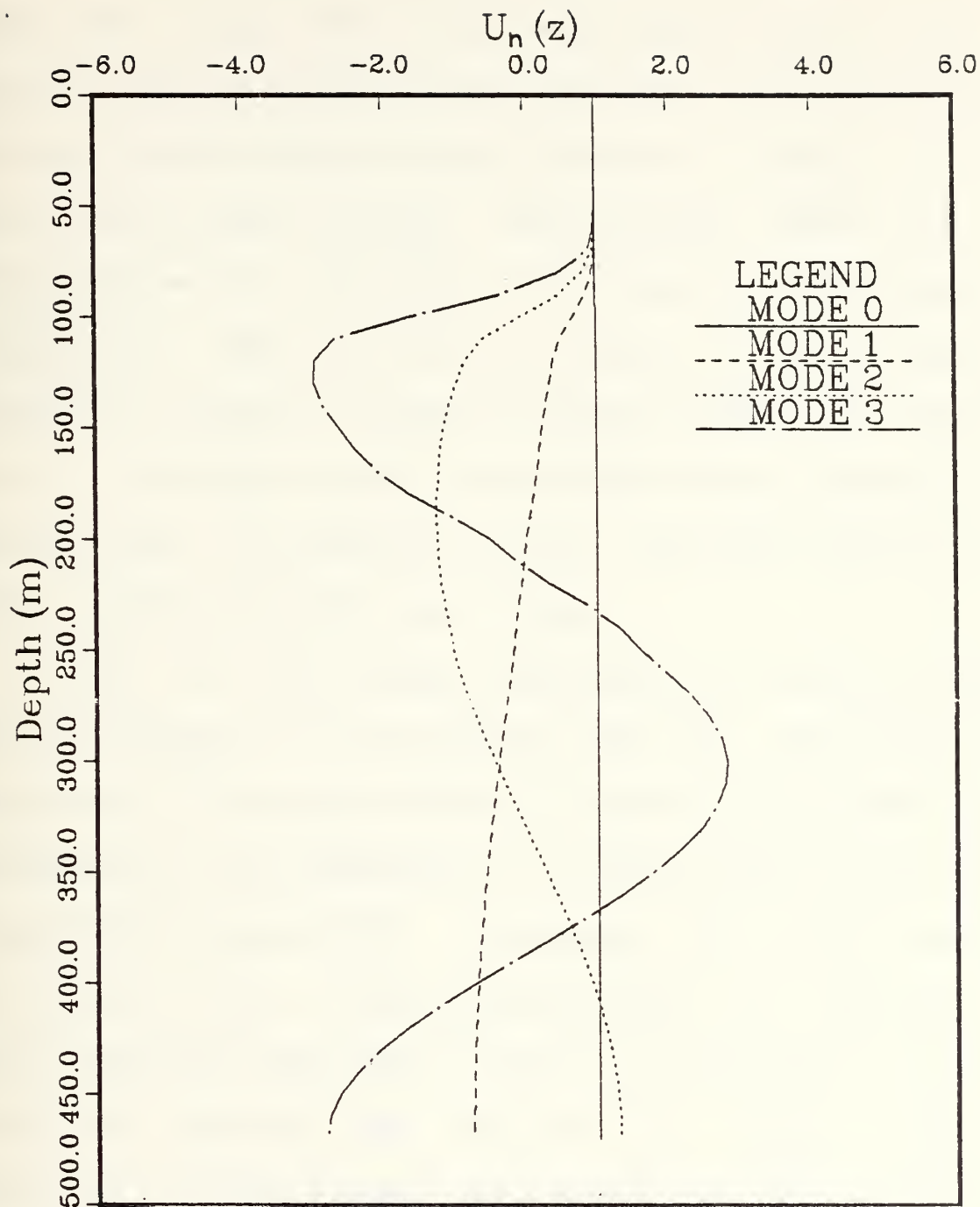


Figure 25. Horizontal Velocity Eigenfunctions at 29.33 N and 87.11 W. The abscissa depicts the amplitude of the horizontal velocity eigenfunction for mode 0 (solid), mode 1 (dashed), mode 2 (dotted) and mode 3 (dashed-dotted).

CMA3 indicates that the storm excited modes 0,1,and 3 with a damped mode 2 (Fig. 26). The amplitudes of modes 0 and 1 reached a peak on JD 256 and then decreased. By JD 262, the barotropic mode horizontal speed decreased to nearly a constant value of about 10 cm/s. After JD 262, modes 0 and 1 oscillated over the remainder of the record with a period of about 5 IP. This behavior of the modes in Fig. 26 indicates that a modulation occurred between inertial wave modes 0 and 1. More importantly, these modes define a modulation envelope which is consistent with the amplitude variations of the currents below the mixed layer.

At CMA2, the time-varying coefficients of the modes are markedly different in their behavior (Fig. 27). The spatial variability in the modal structure between CMA2 and CMA3 is associated with the differences in the mean flow, which is topographically controlled. Initially, all of the modes were excited, with a fairly energetic mode 3. The barotropic coefficient decreased to about 2 cm/s while the mode 1 amplitude approached zero near JD 252. After JD 262, modes 0 and 1 were in phase and defined the limits of the coefficients.

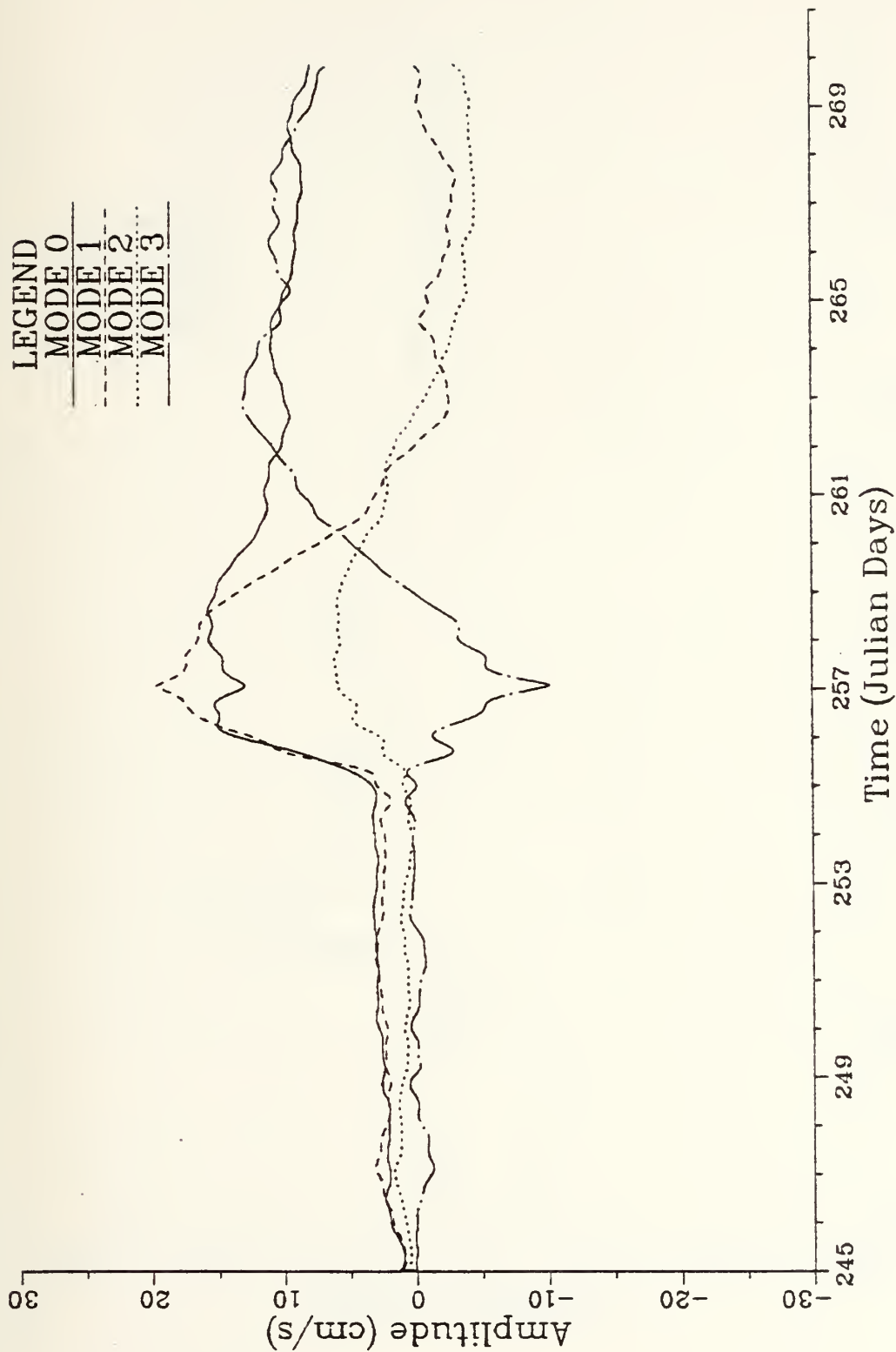


Figure 26. V Velocity Coefficients at CMA3 for mode 0 (solid), mode 1 (dashed), mode 2 (dotted) and mode 3 (dashed-dotted).

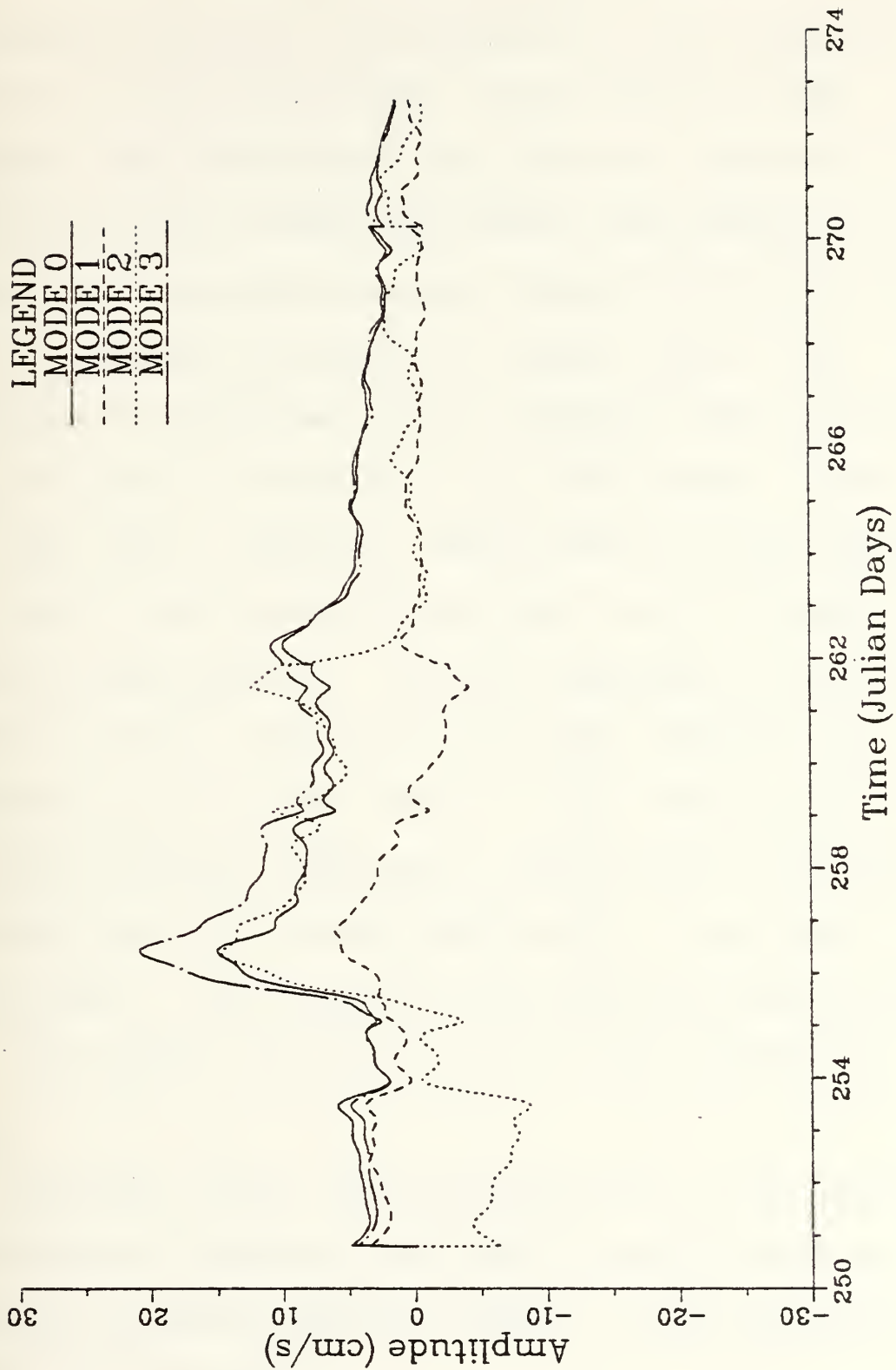


Figure 27. Same as Fig. 26, except at CMA2.

The modal current time series are re-computed using the coefficients from the least squares fit and the eigenfunctions for each of the current meter depths at CMA3. For example, the reconstructed time series are compared in Fig. 28 with the actual demodulated current time series at 251 m. Recall that a secondary maximum occurred at this site about 10 IF following the passage of Frederic (Fig. 10). The reconstructed amplitude of the barotropic mode is greater than the actual v component of the data between JD 255 and 262 (Fig. 28). However, summing modes 0, 1 and 2 accounts for most of the observed variability, with the barotropic mode the most energetic. Over the remainder of the record, JD 262 to 270, most of the observed variability can be described only by modes 0 and 2. The contribution of the barotropic mode was significant and consistent with earlier estimates that the vertical scales were of the order of the water depth. The strength of the barotropic mode continued for the entire time series of the modal coefficients at CMA3.

Estimates of the modal contributions to the observed near-inertial variability are given in Table X for both the storm and poststorm periods at CMA2,3. These estimates are based on the expression

$$s = 1. - \frac{\sum_j (V_j - \hat{V}_{jm})^2}{\sum_j V_j^2} \quad , \quad (12)$$

where V_j and \hat{V}_{jm} are the observed and modal scalar components of the horizontal velocity. The index m depicts the summation of the modes, for example, 0, 0+1, and 0+1+2, and index j represents a summation over the number of observations in the period. The storm period is redefined to start at the time of hurricane passage and continue for 7 IP. The post-storm period starts where the storm period ends and continues for roughly 8 IP until the end of record.

The mixed layer variability at CMA2 is dominated by the barotropic mode during the storm period. The contribution of the barotropic mode to the observed horizontal current variability decreases with depth, but by including the baroclinic modes most of the near-inertial variance can be described by modes 0, 1 and 2. The only exception is at 179 m. The first three modes contribute only 54 and 37% to the observed horizontal current variance in the east-west and north-south directions, respectively. Furthermore, the u-velocity component of the barotropic mode exceeds the

TABLE X

Variance of the Normal Modes at CMA2 and CMA3.

Depth (m)	Velocity Component	Period	Modes		
			0 (%)	0+1 (%)	0+1+2 (%)
<u>CMA2</u>					
19	u	s	68	78	100
19	u	ps	87	91	100
19	v	s	69	78	100
19	v	ps	92	93	100
179	u	s	53	50	54
179	u	ps	98	98	95
179	v	s	35	31	37
179	v	ps	97	98	95
324	u	s	*	50	67
324	u	ps	97	98	99
324	v	s	45	72	85
324	v	ps	97	99	99
<u>CMA3</u>					
21	u	s	69	97	100
21	u	ps	73	86	100
21	v	s	68	98	100
21	v	ps	*	50	100
251	u	s	55	81	98
251	u	ps	95	96	99
251	v	s	58	84	98
251	v	ps	94	95	99
437	u	s	73	68	97
437	u	ps	95	94	91
437	v	s	64	78	94
437	v	ps	94	94	92
457	u	s	22	82	85
457	u	ps	79	74	99
457	v	s	21	89	84
457	v	ps	81	66	99

s: storm period (number of observations = 1008)
 ps: post-storm period (number of observations = 1152)
 *: an overestimation of the variance (explained below)

observations by a considerable amount and causes equation (12) to be less than zero (see Fig. 27). This behavior could be attributed to the bottom boundary layer where infinite energies occur when the slope of the internal wave characteristic approaches the bottom slope (Prinsenberg and Ratnay, 1975). Most of the observed variance during the

post-storm period is attributed to the barotropic mode. The modes are much more well-behaved during this period, which is presumably a manifestation of free waves.

The modes of the horizontal velocity are well-behaved during the storm period at CMA3, except near the bottom where only 20 to 22% of the observed variance can be attributed to the barotropic mode. This is probably due to bottom boundary effects. At the other depths, the barotropic mode explains 55 to 73% of the variance, with most of the variance accounted for by the summation of the barotropic and first two baroclinic modes. During the post-storm period, the observations of the mixed layer velocity are less than that of the barotropic mode in the north-south direction, which causes the value to be less than zero. The reason for this large discrepancy is due to the e-folding scale of the horizontal velocity in the mixed layer, the persistence of the coefficient of the barotropic mode (see Fig. 26), and the radiation of inertial waves away from the storm track. Otherwise, 73 to 95% of the observed horizontal current variance can be attributed to the barotropic mode, and adding the first two baroclinic modes accounts for more than 90% of the variance.

Hopkins (1982) modeled only the baroclinic response to hurricane passage and he found that the inertio-gravity waves decayed too rapidly in the thermocline and bottom layers to account for the vertical structure of the observed variability. Thus, a model with only the baroclinic modes could not explain the secondary maximum observed in these layers.

Some caution has to be applied in the interpretation of the normal modes for several reasons. First, the formulation of the Sturm-Liouville problem assumes that the vertical structure consists of a standing wave for the $N^2 = \text{constant}$ case. From basic physics, a standing wave can be decomposed into two waves of equal amplitudes propagating in opposite directions, which assumes no phase propagation. Over the first 7 to 10 IP, there is a downward propagation of energy, as well as upward propagation of phase, which violates the standing wave argument. Secondly, a flat bottom ocean is assumed for the application of normal mode theory. The validity of this assumption crucially depends on the ratio between the slope of the internal wave characteristic to the bottom slope. For example, as this ratio approaches unity, the energy densities in the bottom boundary layer approach infinity. At

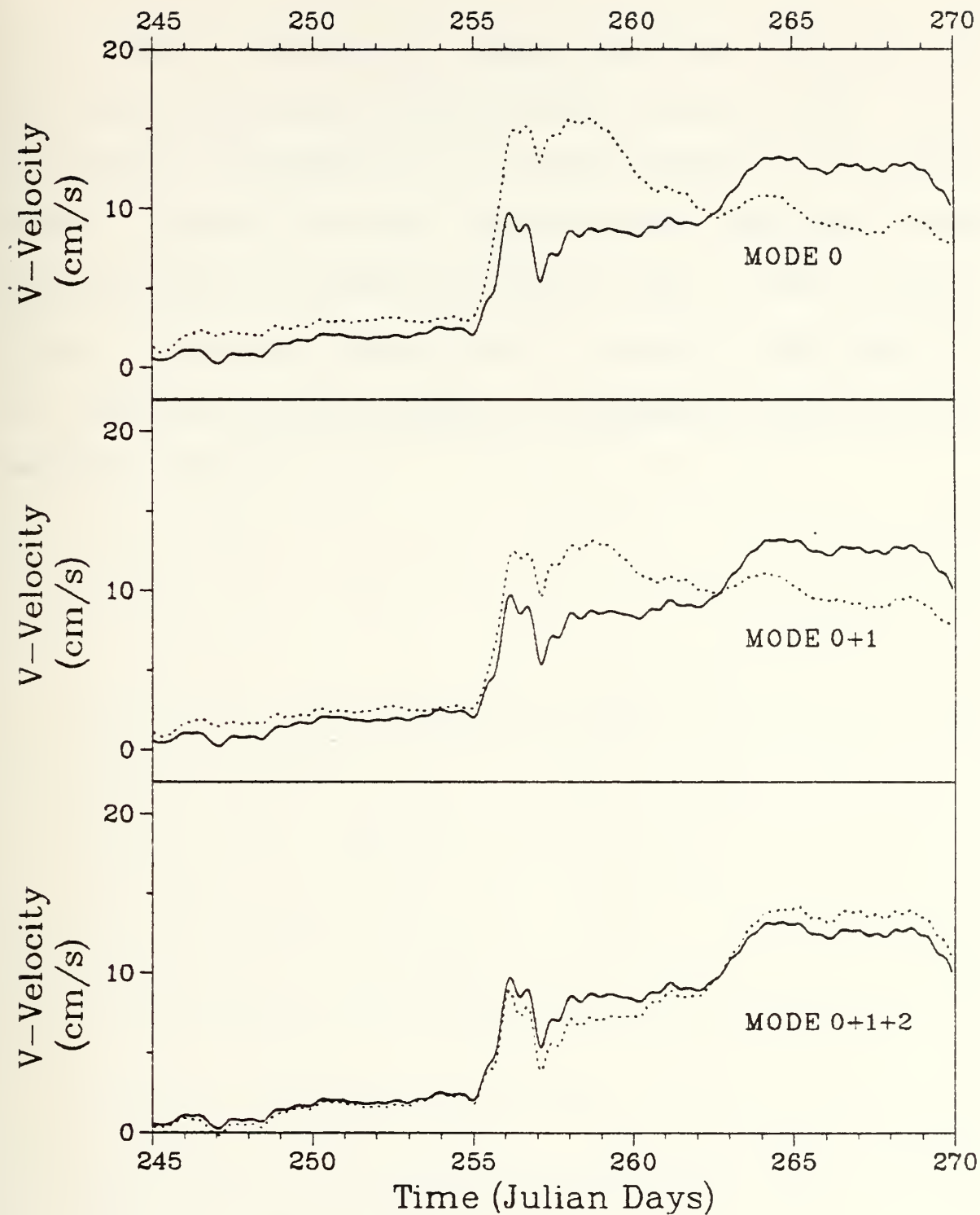


Figure 28. V Component Time Series at CMA3 for the observed time series (solid) and the reconstructed time series (dotted) for a) mode 0 , b) mode 0+1 , c) mode 0+1+2 .

that point, dissipation becomes important and must be included in the model (Prinsenberg and Ratray, 1975). Consequently, the assumption of inviscid dynamics is no longer valid. Despite all these approximations, the normal mode analysis fits the observations quite well. Even the resonance or modulation envelope which occurred at CMA3 about 10 IP following the storm passage, is represented quite well by modes 0,1 and 2.

VI. CONCLUSIONS

The ocean response near the DeSoto Canyon to hurricane Frederic was dominated by the excitation of inertial waves in the mixed layer and inertio-gravity waves in the thermocline. These waves are not admitted onto the shelf because the slope of the characteristics of internal wave motion is less than the bottom slope (Barbee et. al, 1975 ; LeBlond and Mysak, 1978 ; Torgrimson and Hickey, 1979). The major features of the forced inertio-gravity waves observed at CMA2 and 3 are:

- initially, the vertical propagation of energy was of the order of 1. km/d as the forcing was felt throughout the water column within 3 to 4.5 h following the passage of Frederic;
- the initial horizontal propagation of energy was about 80 km/d with a phase speed of 70 cm/s;
- the waves were anisotropic at all depths and had an upward propagation of phase;
- maximum HKE in the mixed layer occurred at the fringe of the maximum wind regime with a second maximum in the thermocline 6 to 10 IP after the storm;
- the EKE decayed on an e-folding scale of about 4 IP after the maximum in the mixed layer and the second maximum in the thermocline;
- the vertical propagation after about 6 IP is of the order of 10^2 m/d with a corresponding horizontal propagation of energy of 30 km/d;
- the mixed layer horizontal scales were 60 and 100 km in the cross and along-track directions, respectively, while the scales in the thermocline were 25 and 50 km in the cross and along-track directions;

- the vertical scales were of the order of the water depth which suggests that the barotropic mode was important;
- most of the observed variability was in the barotropic mode, with some contributions from modes 1 and 2; together they defined a modulation envelope in the deep thermocline at CMA3;
- the modal coefficients varied in space as well as time due to the rugged bottom topography and mean currents.

The mean flow was topographically controlled and reversed direction from surface to bottom. The forced response in the mixed layer caused the mean flow to increase at both CMA2 and CMA3. The mean flow below the mixed layer was also changed by the storm. Furthermore, this mean flow was influenced by subinertial variability (periods of 3 IP) and was linked to the advection of cooler water cross-shelf relative to CMA2.

The semi-diurnal tidal currents increased in magnitude and varied spatially in response to the passage of hurricane Frederic. The near dominance of the semi-diurnal tidal currents over the inertial motions at CMA1 was consistent with internal tide theories. The semi-diurnal tides were admitted to the shelf region because the slope of the internal wave characteristic exceeded the critical bottom slope

(Baines , 1973 ; Prinsenberg and Rattray, 1975 ; Torgrimson and Hickey, 1979) .

In a broader context, the oceanic response to hurricane Frederic was a geostrophic adjustment problem, which had both transient and steady state components. After the transient, inertic-gravity waves propagated away from the storm track, a geostrophically balanced ridge and current system remained under the storm track. That is, the steady state currents were due to the balance between the horizontal pressure gradients and the Coriolis force (Geisler, 1970) . Although some adjustments to the mean flow are described, additional study is required to completely understand the interrelationships between the forced mean flow, the forced wave field and the bottom topography.

APPENDIX A

A. COMPLEX DEMODULATION

The motivation for complex demodulation is to isolate the carrier wave of a certain frequency, which must be known a priori, and to form amplitudes and phases of the modulated signal. A linear filtering approach is used to form the instantaneous amplitudes and phases in contrast to the harmonic analysis method. Essentially, the amplitude and phase time series represents a local harmonic analysis rather than discrete estimates averaged over continuous periods (Otne and Enochson, 1978).

A band-limited time series is multiplied by the trigonometric arguments of the carrier wave. The resultant time series is then low-pass filtered to eliminate some high frequency noise that is generated. The cosine and sine coefficients are then combined to form the amplitude and phase of the modulated wave. Consider the time series:

$$x(i) = A(i) \cos(2\pi f_c \Delta t) + \phi(i) \quad , \quad (1)$$

where f_c is the carrier frequency, Δt is the sampling interval, ϕ is the phase, A is the amplitude of the wave, and i

represents a time index. Both the phase and amplitude vary as functions of time. Multiply equation (1) by the sine and cosine arguments of the carrier frequency f_c ,

$$x_s(i) = A(i) \left\{ \cos((2\pi f_c i\Delta t) + \phi(i)) \right\} \sin(2\pi f_c i\Delta t) , \quad (2)$$

$$x_c(i) = A(i) \left\{ \cos((2\pi f_c i\Delta t) + \phi(i)) \right\} \cos(2\pi f_c i\Delta t) , \quad (3)$$

where

$$x_s(i) = x(i) \sin(2\pi f_c i\Delta t) , \text{ and}$$

$$x_c(i) = x(i) \cos(2\pi f_c i\Delta t) .$$

Equation (2) can be rewritten as

$$x_s(i) = A(i)/2 \left\{ \sin((4\pi f_c i\Delta t) + \phi(i)) \right\} - \sin \phi(i) . \quad (4)$$

Similarly, equation (3) can be expanded and simplified as:

$$x_c(i) = A(i)/2 \left\{ \cos((4\pi f_c i\Delta t) + \phi(i)) \right\} + \cos \phi(i) . \quad (5)$$

Low pass filtering the above x_s , x_c series yields:

$$y_s(i) = -A(i)/2 \left\{ \sin \phi(i) \right\} , \quad (6)$$

$$y_c(i) = A(i)/2 \left\{ \cos \phi(i) \right\} ,$$

where $y_s(i)$ and $y_c(i)$ are the low-pass filtered $x_s(i)$ and $x_c(i)$. These data are filtered by convolving the input series with a set of filter weights in the time domain (Bendat and

Piersol, 1971). Squaring and summing $y_s(i)$ and $y_c(i)$ yields

$$a^2(i) = (y_s^2(i) + y_c^2(i)) = A^2/4$$

or,

$$A(i) = 2 a(i) \quad (7)$$

where $A(i)$ is the amplitude as a function of time. Similarly, the phase as a function of time is computed as:

$$\phi_c(i) = \tan^{-1} (-y_s(i) / y_c(i)) \quad (8)$$

B. POTENTIAL ENERGY

The potential energy is computed to determine the relationship of the isotherm displacements to internal wave motion. Given a temperature time series from a moored array and the corresponding vertical temperature gradient $d\bar{T}/dz$, the isotherm displacement ζ is computed in the following manner:

$$\zeta' = \frac{T'}{d\bar{T}/dz} \quad , \quad (9)$$

where T' is the fluctuating part of the observed temperatures. The potential energy per unit volume is defined by:

$$PE = \frac{\rho_0}{2} N^2 \zeta'^2, \quad (10)$$

where N^2 is the Brunt-Vaisala frequency, ζ' is the isotherm displacement fluctuations, and ρ_0 is the reference density. which is assumed to be unity.

C. LEAST SQUARES FIT

Given a demodulated time series of the amplitude coefficients and the vertical structure of the horizontal velocity eigenfunctions, the problem is to compute the time-varying coefficients associated with each dynamical mode. The time-varying amplitudes $U(z_i, t)$ at depths z_1, z_2, \dots, z_n may be written as

$$U(z_i, t) = \sum_{N=1}^{\infty} C_N(t) E_N(z_i),$$

where $E_N(z_i)$ are the eigenfunctions for modes 1, 2, 3, ..., and $C_N(t)$ are the coefficients to be calculated in the analysis. Only three baroclinic modal coefficients are computed because current meters were deployed at three depths in the water column. For example, the current at depth z_1 , is written as

$$U_1 = C_1 E_1(z_1) + C_2 E_2(z_1) + C_3 E_3(z_1),$$

and there are similar expressions at depth z_2 and z_3 . The square of the error in the least squares fit at depth z_1 is,

$$e_1^2 = \left\{ U_1 - (C_1 E_1(z_1) + C_2 E_2(z_1) + C_3 E_3(z_1)) \right\}^2 \quad (11a)$$

and similarly at z_2 and z_3 ,

$$e_2^2 = \left\{ U_2 - (C_1 E_1(z_2) + C_2 E_2(z_2) + C_3 E_3(z_2)) \right\}^2, \quad (11b)$$

$$e_3^2 = \left\{ U_3 - (C_1 E_1(z_3) + C_2 E_2(z_3) + C_3 E_3(z_3)) \right\}^2. \quad (11c)$$

The error is minimized by solving the following set

$$\partial e_1^2 / \partial C_1 + \partial e_2^2 / \partial C_1 + \partial e_3^2 / \partial C_1 = 0, \quad (12a)$$

$$\partial e_1^2 / \partial C_2 + \partial e_2^2 / \partial C_2 + \partial e_3^2 / \partial C_2 = 0, \quad (12b)$$

$$\partial e_1^2 / \partial C_3 + \partial e_2^2 / \partial C_3 + \partial e_3^2 / \partial C_3 = 0. \quad (12c)$$

Differentiating equation (11) with respect to C_1 and summing the expressions according to equation (12a) yields

$$U_1 E_1(z_1) + U_2 E_2(z_2) + U_3 E_3(z_3) =$$

$$\begin{aligned} & C_1 (E_1(z_1) E_1(z_1) + E_1(z_2) E_1(z_2) + E_1(z_3) E_1(z_3)) \\ & + C_2 (E_1(z_1) E_2(z_1) + E_1(z_2) E_2(z_2) + E_1(z_3) E_2(z_3)) \\ & + C_3 (E_1(z_1) E_3(z_1) + E_1(z_2) E_3(z_2) + E_1(z_3) E_3(z_3)), \end{aligned}$$

or

$$\sum_{i=1}^3 U_i E_1(z_i) = C_1 \sum_{i=1}^3 E_1(z_i) E_1(z_i) + C_2 \sum_{i=1}^3 E_1(z_i) E_2(z_i)$$

$$+ C_3 \sum_{i=1}^3 E_1(z_i) E_3(z_i) \quad . \quad (13)$$

Now if equations (12b,c) are applied to equations (11), the corresponding equations for C_2 and C_3 become:

$$\begin{aligned} \sum_{i=1}^3 U_i E_2(z_i) &= C_1 \sum_{i=1}^3 E_1(z_i) E_2(z_i) + C_2 \sum_{i=1}^3 E_2(z_i) E_2(z_i) \\ &+ C_3 \sum_{i=1}^3 E_3(z_i) E_2(z_i) \quad , \end{aligned} \quad (14)$$

$$\begin{aligned} \sum_{i=1}^3 U_i E_3(z_i) &= C_1 \sum_{i=1}^3 E_1(z_i) E_3(z_i) + C_2 \sum_{i=1}^3 E_2(z_i) E_3(z_i) \\ &+ C_3 \sum_{i=1}^3 E_3(z_i) E_3(z_i) \quad . \end{aligned} \quad (15)$$

By inspection, let

$$\alpha_{mn} = \sum_{i=1}^3 E_m(z_i) E_n(z_i) \quad \text{for } m,n = 1,2,3 \quad , \quad (16)$$

$$\beta_m = \sum_{i=1}^3 U_i E_m(z_i) \quad . \quad (17)$$

Therefore, equations (13-15) can be simplified using the above definitions into a simple matrix equation of the form

$$\beta_m = \alpha_{mn} \cdot C_n \quad . \quad (18)$$

Equation (18) is a simple symmetric matrix equation and it was solved using the IMSL routine LEQT2F on the IBM 3033.

APPENDIX E

A. DEEP REGION

The ocean currents at CMA2,3 during the quiescent period clearly showed topographical effects associated with the DeSoto Canyon. The behavior of the surface currents is best described by a FVD (Fig. 29). The strong u component at CMA2 produced a total displacement of 600 km over 39 days for a 15.4 km/d mean current. Inertial waves were superposed on this mean flow, particularly during the period from JD 232 to 239. The mean flow increased during this period. At CMA3, the mean flow decreased in the southerly direction from 13.3 to 9.5 km/d (Fig. 29b). The different orientation in the mean flow across the entire shelf region is presumably due to the influence of bottom topography.

The trajectory of the near-bottom horizontal currents at CMA2 (Fig. 30a) was in the same direction as in the mixed layer until JD 232. After the reversal, the mean flow was towards the west at about 3.3 km/d. The bottom PVD at CMA3 (Fig. 30b) showed that initially the mean flow was towards the north at 2.0 km/d over the first 6 IP. The flow then

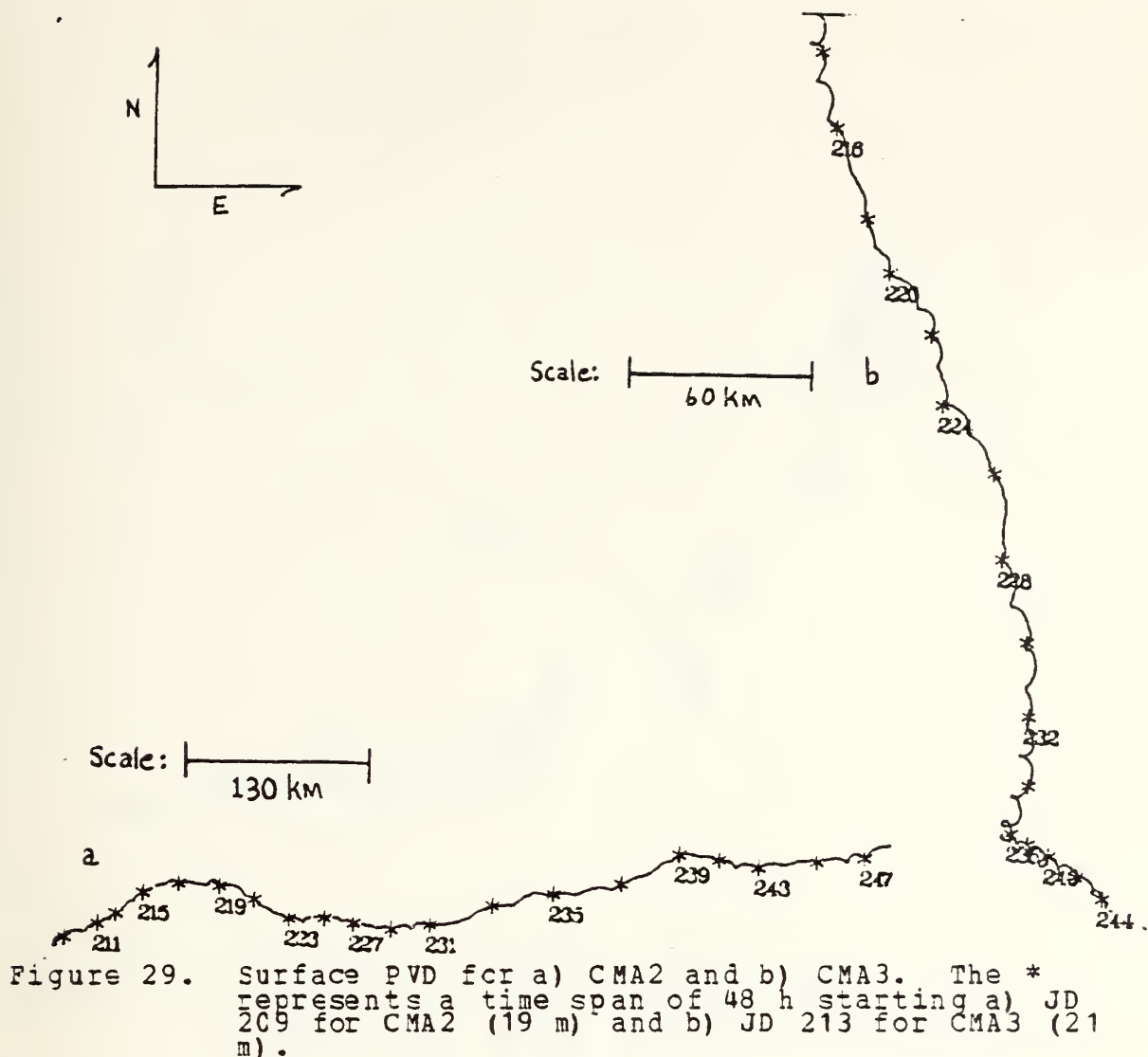


Figure 29. Surface PVD for a) CMA2 and b) CMA3. The * represents a time span of 48 h starting a) JD 209 for CMA2 (19 m) and b) JD 213 for CMA3 (21 m).

changed direction and accelerated to about 2.8 km/d in the same direction as in the surface layer.

Horizontal kinetic energy spectra for this period are summarized in Table XI for both inertial and semi-diurnal frequency bands. The vertical variation in the inertial HKE levels at CMA2 indicated a larger amount of energy in the

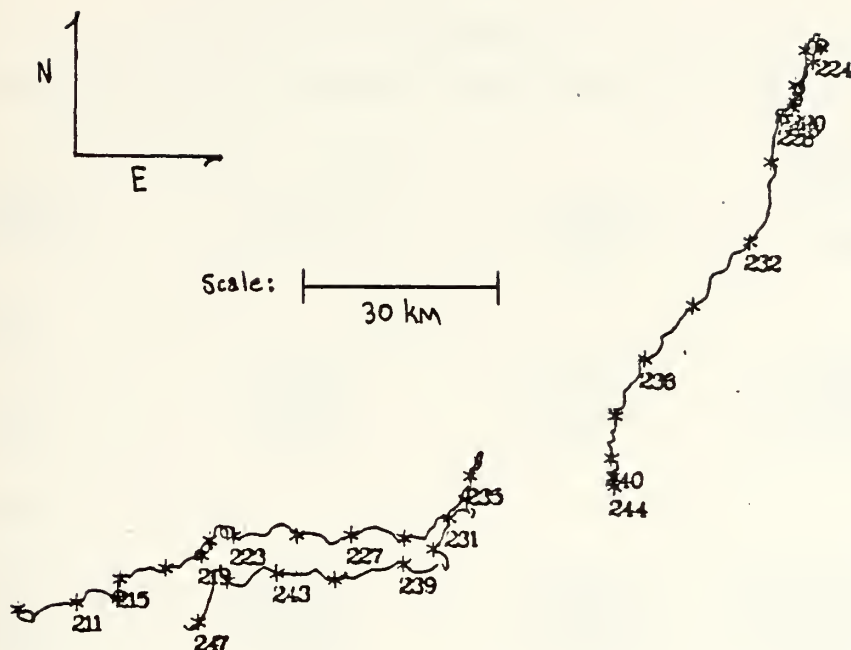


Figure 30. Bottom PVD for a) CMA2 and b) CMA3. The * represents a time span of 48 h starting a) JD 209 for CMA2 (324 m) and b) JD 213 for CMA3 (457 m).

thermocline than at the surface or near-bottom. However, the difference between the surface and bottom energy levels was about one order of magnitude. At CMA3, the inertial HKE estimates decreased steadily with depth and there was more than an order of magnitude difference between the surface and bottom layers. The HKE levels were slightly greater at

CMA3 in the surface layer and thermocline, but they were slightly less near the bottom than at CMA2.

TABLE XI
Normalized HKE Spectral Estimates at 95% Confidence

Meter Depth (m)	No. of Data Points	Bandwidth cph	Normalized HKE Spectra f	M2 (cm/s) ² /cph
a) CMA2				
19	5780	0.001	$1.7 \times 10^{+3}$	$2.1 \times 10^{+2}$
179	4590	0.0013	$3.0 \times 10^{+3}$	$3.8 \times 10^{+1*}$
324	5780	0.001	$3.1 \times 10^{+2}$	$8.0 \times 10^{+1*}$
b) CMA3				
21	4680	0.0013	$8.0 \times 10^{+3}$	$2.3 \times 10^{+3}$
251	4680	0.0013	$4.5 \times 10^{+3}$	$7.0 \times 10^{+2}$
437	4680	0.0013	$1.9 \times 10^{+3}$	$4.6 \times 10^{+3}$
457	4680	0.0013	$2.0 \times 10^{+2}$	$1.7 \times 10^{+1}$

* instrumentation problems with time clock
M2 is the semi-diurnal tide frequency band
f is the inertial/diurnal tide frequency band

The semi-diurnal HKE estimates also varied spatially. The estimates of HKE in the thermocline and near-bottom layers at CMA2 were not significant; however, the HKE estimates at CMA3 were significant at all depths. The HKE estimates at 437 m even exceeded both the surface layer and thermocline levels by about an order of magnitude. In comparison with the near-bottom estimates at 457 m, the kinetic energy

levels were more than two orders of magnitude greater. These pronounced changes in the semi-diurnal energy levels with depth indicate the presence of internal tide motion. In most of the kinetic energy spectra examined, longer period motions were insignificant, because their energies were smeared across adjacent bands except in the bottom layers. Subinertial variability at periods of about 3 IP was quite apparent in the bottom records at both CMA2 and CMA3. These motions were generally more energetic than the semi-diurnal tides.

Rotary spectra are analyzed for the surface and bottom current records and are given in Table XII. Most of the HKE variability is consistent with polarized, CW rotating inertial motions. The CW energy level exceeds the CCW level by about an order of magnitude. The ellipse orientations for these waves rotates CCW (backs) with depth. These ellipses are stable except for the near-bottom inertial period motion at CMA2. The direction of the semi-major axis of the ellipse varies over time, which indicates that the inertial waves are isotropic. The semi-diurnal tidal motion is polarized in the CW direction. Generally, the semi-diurnal tidal motions are coherent, although the phase differences

between the horizontal velocity components vary between the arrays.

TABLE XII
Normalized Rotary Spectrum Analysis

Freq. Band	Depth (m)	Normalized Rotary Spectra		Ellipse Stab.	Dir. (Deg.)	Rotary Coeff.
		CW (cm/s)	CCW +2/cph			
a) <u>CMA2</u>						
I	19	$1.6 \times 10^{+3}$	$1.9 \times 10^{+2}$	0.80	103	+0.90
S	19	$1.6 \times 10^{+2}$	$3.6 \times 10^{+1}$	0.39	101	+0.87
I	324	$5.0 \times 10^{+2}$	$1.4 \times 10^{+1}$	0.05	90	+0.87
S	324	$1.0 \times 10^{+0}$	$1.1 \times 10^{+0}$	0.60	169	-0.18
b) <u>CMA3</u>						
I	21	$1.2 \times 10^{+4}$	$1.7 \times 10^{+1}$	0.40	157	+0.99
S	21	$4.0 \times 10^{+2}$	$3.0 \times 10^{+1}$	0.61	55	+0.63
I	457	$5.6 \times 10^{+2}$	$1.6 \times 10^{+1}$	0.51	138	+0.96
S	457	$3.0 \times 10^{+1}$	$3.9 \times 10^{+0}$	0.20	93	+0.75

I=inertial frequency band
S=Semi-diurnal frequency band

Ocean bottom temperatures ranged between 8.0 and 12.5 °C at CMA2 and 8.0 to 9.0 °C at CMA3 (Fig. 31), but there were different variations and trends. At CMA2, (not shown) the temperature decreased gradually to about 8.3 °C near JD 234, and then increased abruptly without any periodicities. Bottom temperatures at CMA3 were much lower and there was near-inertial motion superposed on this early cooling trend.

The minimum temperature occurred on JD 232, which was about 2 IP before the minimum observed at CMA2. These minima in the temperature, in addition to the cooling trends, are manifestations of the advection of cold water from the DeSoto Canyon by the mean flow.

B. SHALLOW REGION

In the thermocline (49 m), the inertial oscillations were not nearly as energetic and did not rotate CW as in the mixed layer (Fig. 32). The non-stationary trends in the east-west currents were similar to the mixed layer observations, but there was an initial mean flow towards the deep ocean. Superposed on the mean flow were lower frequency oscillations with periods of the order of about 10 to 14 IP. The total displacement over the forty days was about 300 km which corresponded to a mean current of 7.5 km/d.

Inertial oscillations at 64 m were not as energetic as at 49 m, but there was a similar non-stationary trend in the time series. This trend was associated with a lower frequency waves having a period of 10 to 14 IP. These oscillations were superposed on a northward mean flow which was slightly less than 7.0 km/d. Records from the current meter nearest to the bottom (92 m), were out of synchronization



Figure 31. Temperature Time Series from CMA3 at 457 m.

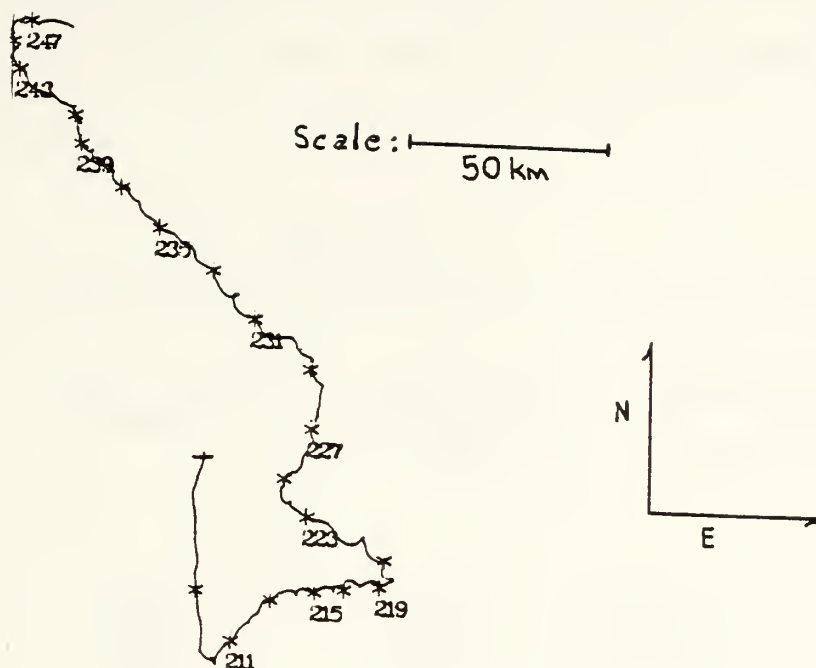


Figure 32. Mid-depth PVI at CMA1. The * represents a time span of 48 h starting on JD 207 at 49 m.

due to internal clock problems. For example, large increases in the velocity occurred on JD 252 as opposed to 256. Hence, the data were not included.

The HKE spectra for the 21, 49, and 64 m depths are shown in Table XIII for both the inertial and semi-diurnal frequency bands. The inertial/diurnal tidal kinetic energy

in the surface layer was two orders of magnitude larger than in the subsurface layers. The semi-diurnal tidal motion decreased from the surface to 49 m and then increased with depth such that the HKE near the bottom almost equaled that near the surface.

TABLE XIII

Normalized HKE Spectral Estimates at 95% Confidence

Meter Depth (<u>m</u>)	No. of Data Points	Frequency Resolution <u>cph</u>	Normalized HKE Spectra f M2 (<u>cm/s</u>) ⁺² / <u>cph</u>	
<u>CMA1</u>				
21	5825	0.001	1.4x10 ⁺⁴	1.5x10 ⁺²
49	5825	0.001	1.4x10 ⁺³	4.3x10 ⁺¹
64	5825	0.001	5.0x10 ⁺²	8.0x10 ⁺¹
92*	5825	0.001	1.5x10 ⁺²	1.0x10 ⁺²

* instrumentation problems with time clock
M2 is the semi-diurnal tide frequency band
f is the inertial/diurnal tide frequency band

Temperature data at both 21 and 49 m are not available because of the thermistor problem. The temperatures ranged from 18.0°C to the thermistor cutoff of 21.5 °C at 49 m. Temperature variations were about 0.5°C over an IP, although most of the variability was associated with some non-stationary trends and lower frequency motions similar to those observed in the currents. Just prior to the storm, tempera-

tures decreased to a relative minimum as cold water was advected by the mean flow.

In summary, based on the observations during the quiescent period, the mean flow strongly depends on the bottom topography. Inertial band motion is evident at all depths during the quiescent period. Some of this motion is due to freely propagating inertial waves while the remainder is part of the forced diurnal tides. Internal tides, as well as inertial oscillations, are part of the freely propagating internal wave continuum below the surface layer. The effect of the topography on the mean flow and the wave motions further complicates the dynamics of the region and the resultant circulation. Longer period waves (2.5 to 3 day period) set up north-south oscillations that advect cooler water from the DeSoto Canyon onto the shelf region. Super-inertial frequency motions are influenced by the diurnal and semi-diurnal tides and contribute to the variability.

LIST OF REFERENCES

Adamec, D., R. L. Elsberry, R. W. Garwood Jr., and R. L. Haney, 1980, An embedded mixed-layer ocean circulation model, Dyn. of Atmos. and Oceans, 6, 69-96.

Baines, P. G., 1971, The reflection of internal/inertial waves from bumpy surfaces, J. Fluid Mech., 46, 273-291.

Baines, P. G., 1973, The generation of internal tides by flat-bump topography, Deep-Sea Res., 20, 179-205.

Barbee, W. D., J. G. Dworski, J. D. Irish, L. H. Larson, and M. Rattray Jr., 1975, Measurement of internal waves of tidal frequency near a coastal boundary, J. Geophys. Res., 15, 1965-1974.

Bell, T. H., 1978, Radiation damping of inertial oscillations in the upper ocean, J. Fluid Mech., 88, 289-305.

Bendat, J. S., and A. G. Piersol, 1971, Random Data: analysis measurement procedures, Wiley-Interscience, New York, 407 pp.

Black, P. G., 1983, Ocean temperature changes induced by tropical cyclones, Ph. D. dissertation, The Pennsylvania State Univ., 278pp.

Brooks, D., 1983, The wake of hurricane Allen in the western Gulf of Mexico, J. Phys. Oceanogr., 13, 117-129.

Elsberry, R. L., T. Fraim, and R. Trapnell, 1976, A mixed layer model of the ocean thermal response to hurricanes J. Geophys. Res., 81, 1153-1162.

Fjeldstad, J. E., 1958, Ocean current as an initial problem, Geophysiske Pub., 20(7), 1-24.

Fofonoff, N. F. and Y. Ercan, 1967, Response characteristics of a savonius rotor current meter, Woods Hole Oceanographic Institution, WHCI ref. no. 67-33,

Fu, L-L., 1981, Observations and models of inertial waves in the deep ocean, Rev. Geophys. Space Phys., 19(1), 141-170.

Garwood, R. W., Jr., 1977, An oceanic mixed-layer model capable of simulating cyclic states, J. Phys. Oceanogr., 7, 455-468.

Geisler, J. E., 1970, Linear theory on the response of a two layer ocean to moving hurricane, Geophys. Fluid Dyn., 1, 249-272.

Gerald, C. F., 1980, Applied Numerical Analysis, Addison-Wesley, Reading, Massachusetts, 518 pp.

Gonella, J., 1972, A rotary component method for analyzing meteorological and oceanographic time series, Deep-Sea Res., 19, 833-846.

Greatbatch, R. J., 1983, On the response of the ocean to a moving storm: the nonlinear dynamics, J. Phys. Oceanogr., 13, 357-367.

Hebert, P., 1979, Preliminary report: hurricane Frederic Aug 29 - Sept. 14, 1979, NOAA National Hurricane Center, Miami, Florida.

Hopkins, C., 1982, Ocean response to hurricane forcing, M. S. Thesis, Naval Postgraduate School, Monterey, California, 89 pp.

Johnson, A. and S. Renwick, 1981, Buoy observations during the passage of hurricane Frederic 1979, Data Report, NOAA Data Buoy Office, NSTL Station, Mississippi.

Kase, R. H. and D. J. Olbers, 1979, Wind driven inertial waves observed during phase III of GATE, Deep-Sea Res., 26I, 191-216.

Krauss, W., 1972, Wind generated internal waves and inertial periodic motion, Dtsch. Hydrogr. Z., 25, 241-250.

Krauss, W., 1976a, On currents, internal and inertial waves in a stratified ocean due to variable winds, Part 1, Dtsch. Hydrogr. Z., 29, 87-96.

Krauss, W., 1976a, On currents, internal and inertial waves in a stratified ocean due to variable winds, Dtsch. Hydrogr. Z., 29, 121-135.

LeBlond, P. H. and L. A. Mysak, 1978, Waves in the ocean, Elsevier, Amsterdam, 638 pp.

Leipper, D., 1967, Observed ocean conditions and hurricane Hilda, 1964, J. Atmos. Sci., 24, 182-196.

Mayer, D., M. C. Mofjeld, and K. D. Leaman, 1981, Near-inertial internal waves on the outer shelf in the middle Atlantic Bight in the wake of hurricane Belle, J. Phys. Oceanogr., 11, 86-106.

McComas, C. H. and F. P. Bretherton, 1977, Resonant interactions of oceanic internal waves, J. Geophys. Res., 82, 1397-1412.

Mooers, C. N. K., 1973, A technique for the cross spectrum analysis of complex valued time series with emphasis on properties of polarized components and rotational invariants, Deep-Sea Res., 20, 1129-1141.

O'Brien, J. and R. O. Reid, 1967, The nonlinear response of a two layer baroclinic ocean to a stationary, axially-symmetric hurricane, I, Upwelling induced by momentum transfer, J. Atmos. Sci., 24, 208-215.

Otnes, R. K., and L. Enochson, 1978, Applied Time Series Analysis, Wiley-Interscience, New York, pp. 449.

Perkins, H., 1970, Inertial oscillations in the Mediterranean Sea, Ph.D. dissertation, Massachusetts Institute of Technology, Woods hole Oceanographic Institution, 123 pp.

Pollard, R. T., 1970, On the generation by winds of inertial waves in the ocean, Deep-Sea Res., 17, 795-812.

Pollard, R. T., 1980, Properties of near-surface inertial oscillations, J. Phys. Oceanogr., 10, 385-398.

Pollard, R. T. and R. C. Millard, 1970, Comparison between observed and simulated wind generated inertial oscillations, Deep Sea Res., 17, 813-821.

Pollard, R. T., F. B. Rhines, and R. Thompson, 1973, The deepening of the wind mixed layer, Geophys. Fluid Dyn., 3, 381-404.

Price, J., 1983, Internal wave wake of a moving storm, Part I, scales, energy budget and observations, J. Phys. Oceanogr., 13, 949-965.

Prinsenberq, S. J., and M. Rattray, Jr., 1975, Effects of continental slope and variable Brunt-Vaisala frequency on the coastal generation of internal tides, Deep-Sea Res., 22, 251-263.

Shay, L. K. and J. J. Tamul, 1980, Abstract: Current observations in the wake of hurricane Frederic, EOS, vol. 61(17), p.256.

Torgrimson, G. M., and B. Hickey, 1979, Barotropic and baroclinic tides over the continental slope and shelf off Oregon, J. Phys. Oceanogr., 9, 945-961.

Wang, Dong-Ping, and C. N. K. Mooers, 1976, Coastal trapped waves in a continuously stratified ocean, J. Phys. Oceanogr., 6, 853-863.

INITIAL DISTRIBUTION LIST

	No. Copies
1. Defense Technical Information Center Cameron Station Alexandria, VA 22314	2
2. Library, Code 0142 Naval Postgraduate School Monterey, CA 93943	2
3. Professor Robert J. Renard, Code 63Rd Department of Meteorology Naval Postgraduate School Monterey, CA 93943	1
4. Professor Christopher N. K. Mooers, Code 68Mr Department of Oceanography Naval Postgraduate School Monterey, CA 93943	1
5. Professor Russell L. Elsberry, Code 63Es Department of Meteorology Naval Postgraduate School Monterey, CA 93943	4
6. Dr. Andrew Willmott, Code 68W Department of Mathematics University of Exeter North Park Road Exeter EX4 4QE England	1
7. Dr. William Hart, Code 8000 Naval Oceanographic Office NSTL Station Bay St. Louis, MS 39522	1
8. Mr. Lynn K. Shay, Code 63 Dept. of Meteorology Naval Postgraduate School Monterey, CA 93943	2
9. Director Naval Oceanography Division Naval Observatory 34th and Massachusetts Avenue NW Washington, D.C. 20390	1
10. Commander Naval Oceanography Command Central NSTL Station Bay ST. Louis, MS 39522	1

11. Commanding Officer 1
Naval Oceanographic Office
NSTL Station
Bay St. Louis, MS 39522
12. Commanding Officer 1
Fleet Numerical Oceanography Center
Monterey, CA 93940
13. Commanding Officer 1
Naval Ocean Research and Development
Activity
NSTL Station
Bay ST. Louis, MS 39522
14. Commanding Officer 1
Naval Environmental Prediction Research
Facility
Monterey, CA 93940
15. Chairman, Oceanography Department 1
U.S. Naval Academy
Annapolis, MD 21402
16. Chief of Naval Research 1
800 N. Quincy Street
Arlington, VA 22217
17. Office of Naval Research (Cde 480) 1
Naval Ocean Research and Development
Activity
NSTL Station
Bay ST. Louis, MS 39522
18. Scientific Liaison Office 1
Office of Naval Research
Scripps Institution of Oceanography
La Jolla, CA 92037
19. Library 1
Scripps Institution of Oceanography
P.O. Box 2367
La Jolla, CA 92037
20. Library 1
Department of Oceanography
University of Washington
Seattle, WA 98105
21. Library 1
CICESE
P.O. Box 4803
San Ysidro, CA 92073

- 22. Library 1
School of Oceanography
Oregon State University
Corvallis, OR 97331
- 23. Library 1
Coastal Studies Institute
Louisiana State University
Eaton Rouge, LA 70603
- 24. Commander 1
Oceanographic Systems Pacific
Box 1390
Pearl Harbor, HI 96860
- 25. Commander (Air-370) 1
Naval Air Systems Command
Washington, D. C. 20360
- 26. Chief, Ocean Services Division 1
National Oceanic and Atmospheric
Administration
8060 Thirteenth Street
Silver Springs, MD 20910

207664

Thesis
S437365 Shay
c.1

Observations of in-
ertio-gravity waves in
the wake of hurricane
Frederic.

207664

Thesis
S437365 Shay
c.1

Observations of in-
ertio-gravity waves in
the wake of hurricane
Frederic.



thesS437365

Observations of inertio-gravity waves in



3 2768 001 94402 8

DUDLEY KNOX LIBRARY